LLNL-JRNL-818763

LAWRENCE LIVERMORE NATIONAL LABORATORY

On the emergence of human influence on surface air temperature changes over India

R. Dileepkumar, K. AchutoRao, C. Bonfils, T. Arulalan

January 26, 2021

Journal of Geophysical Research - Atmospheres

Disclaimer

On the emergence of human influence on surface air temperature changes over India.

Dileepkumar R.[1], Krishna AchutaRao[1], Céline Bonfils[2] , Arulalan T. [1,3]

[1] Department of Mathematics, KSMDB College, Sasthamcotta, Kerala
[2]Centre for Atmospheric Sciences, Indian Institute of Technology Delhi
[3]Lawrence Livermore National Laboratory
[4]India Meteorological Department, Ministry of Earth Sciences, Government of India

Key Points:

1. The observed variations in temperature are inconsistent with unforced variability at the 1% significance level.
2. The increase in temperature is mainly due to increases in greenhouse gases but partially offset by anthropogenic aerosols.

Abstract

Human activities in terms of greenhouse gas emissions and aerosols resulting from the combustion of fossil fuels have been shown to have affected the temperature of the Earth on global and continental scales. The surface air temperature over India has also been observed to be increasing over the last 100 years. Understanding the underlying causes of regional climate change over India can help in developing appropriate mitigation and adaptation strategies. Differentiating signals of externally forced climate changes from the noise of natural internal variability generally becomes more difficult as spatial scale reduces. Therefore detecting and attributing the influence of external forcings such as greenhouse gases and aerosols is harder at local and regional scales. In this study, we applied a detection and attribution (D&A) method to study annual and seasonal mean surface air temperature over the Indian region. We found that the observed warming over India from 1906 to 2005 cannot be explained by natural climate variability alone. We found that the warming is largely driven by the increase in greenhouse gases, and partially offset by regional anthropogenic emissions of aerosols. These results were confirmed for the shorter 1956-2005 period, but results were sensitive to the choice of observational dataset. The changes cannot be explained by internal climate variability or natural external forcings alone, but are compatible with the responses to combined anthropogenic greenhouse gas and aerosol forcings.

Plain Language Summary

Understanding the nature and causes of near-surface temperature change at regional scales can help policymakers at the regional levels in making informed adaptation and mitigation policies. Surface air temperature over India has been observed to be increasing over the last 100 years. Here, we use a pattern-based fingerprint technique to look for time-increasing spatial correspondence between the observed changes in surface temperature over continental India over the 1906-2005 period (as well as the 1956-2005

period for which multiple observational datasets were available). We examine both the annual mean changes, as well as the changes in individual seasons, and find, in all cases, a detectable human influence in the observed temperature changes over India.

Index Terms

Climate change and variability (3305), Regional climate change (1637)

Key words

Fingerprint, Detection-Attribution, anthropogenic, regional climate change

1. Introduction

Numerous studies have shown significant changes in observed temperature and rainfall over the Indian subcontinent during the 20th century. Kothawale and Rupa Kumar (2005) quantified the increasing trend in annual mean temperature over the Indian region by 0.05°C/decade during the period 1901-2003. Attri and Tyagi (2010) found that the annual mean temperature of Indian region has risen at a similar average rate, by 0.56°C during the 1901-2009 period. Srivastava et al. (2017) report that the annual mean, maximum and minimum temperatures of India have increased significantly during the period 1901–2010 by about 0.6, 1.0 °C and 0.18°C per century, respectively. They showed an accelerated warming trend in maximum and minimum temperature during the 1981–2010 period, and this warming trend is particularly seen over the central, northern, and eastern/northeastern parts of the country. Using the CMIP5 (Coupled Model Intercomparison Project 5; Taylor et al., 2012) model archive, Sonali and Kumar (2016) analysed changes in maximum and minimum temperatures and detected a significant change in observed minimum temperatures over India but could not attribute it to specific forcings.

Many detection and attribution (D&A) analyses of surface air temperature (TAS) changes have been performed at global and continental scales (Jones et al., 2013; Stott et al., 2001, 2000; Tett et al., 2002, 1999; Zhou and Tung, 2013). On global scales, anthropogenic aerosols were found to partially offset the influence of Greenhouse gas (GHG) forcings on surface temperature warming (Jones et al., 2011). Global mean surface air temperature changes have also been attributed to anthropogenic forcings without using General Circulation Models (Triacca et al., 2013; Pasini et al., 2017; Mazzocchi and Pasini, 2017) . Those results also show that a substantial increase in the global temperature of the last half-century might be attributed primarily to anthropogenic forcings. Over regional scales, the detection and attribution of externally forced climate change studies is more challenging. The main difficulties are due to the poorer ability of global models to reproduce climate statistics of the regional scale and to the lack of high-resolution observational datasets. The amplitude of internal variability is also larger over regional scales resulting in a reduction of the signal-to-noise (S/N) ratio - thereby limiting the identification of external factors. The influence of regionally important forcings such as land-use change, irrigation, aerosols, etc. also adds to the uncertainty (Bonfils et al. 2008b). Recently, there has been considerable (and increasing) evidence for anthropogenic influence on other variables in climate (Santer et al.,2013, 2018) and at regional scales (e.g., Bonfils et al. 2008a, Bindoff et al., 2013; Gray et al., 2014; Henson et al., 2018; Mueller et al., 2018; Slangen et al., 2016; Undorf et al., 2018). At regional scale, the masking influence of anthropogenic aerosols can be even larger. Pasini and Modugno (2013) performed a regional-scale D&A study over the Alpine region of Europe using nonlinear analysis, and attributed changes to the direct role of anthropogenic forcings and showed the influence of natural forcings to be negligibly small. Dileepkumar et al. (2018) (referred hereafter as DKA) analyzed spatially averaged TAS changes for different seasons over homogeneous temperature zones of India and attributed the changes between 1956–2005 to GHG forcing with other anthropogenic forcings (that include anthropogenic aerosols and land use changes) partially offsetting the GHG-induced changes.

The D&A study in DKA used regression-based methods applied to sub-regions of India. One of the shortcomings of the study was the inability to separate the effect of anthropogenic aerosols from other (non-GHG) anthropogenic responses. Marvel et al. (2015) and Shiogama et al. (2013) employed single-forcing simulations and tested the validity of linear additivity of climate responses to various individual forcings. They found that the linearity hypothesis is verified for temperature (but not necessarily valid for precipitation).

In this study, we employed a pattern-based D&A method (Marvel and Bonfils, 2013) to analyze the spatial pattern of responses to the individual or combined forcings and separate natural and human contributions in the observed temperature changes over the Indian subcontinent.

2. Observed and model data

We used a publicly available long term dataset of observed (OBS) monthly mean near surface (2m) temperature CRU-3.22 (Harris et al., 2014) gridded (0.5°x0.5° resolution) dataset available from 1901 to 2013 (https://crudata.uea.ac.uk/cru/data/hrg/cru_ts_3.22/). We regridded the CRU 3.22 dataset to 1°x1° resolution and masked out all but the Indian land area. The dataset was time-averaged to produce annual, and seasonal means. To test the sensitivity of our detection results to observational uncertainties, a second dataset from the India Meteorological Department (IMD) - a 1^{o}x1^{o} degree gridded daily temperature data available from 1956 to 2018 (Srivastava et al. 2009) was also considered. Basha et al. (2017) compared the CRU and IMD datasets for consistency over the 1969 to 2005 period and found that CMIP5 simulations seem to be more comparable with CRU observations than with IMD data. Given the shorter length of the dataset and its problems documented in Basha et al. (2017), the major part of our analysis is restricted to the CRU dataset, but IMD observations are also analyzed and discussed for the common period of coverage between the two datasets.

Monthly average TAS (mean surface air temperature) from the control simulations (‘piControl’; pre-industrial control simulations (CTL)), and from the diverse historical simulations (‘historical’ for the simulations of the historical climate forced with the best estimates of all combined forcings (ALL); ‘historicalNat’ to naturally forced volcanic and solar changes alone (NAT); ‘historicalAnt’ the simulations forced by the combined anthropogenic GHG and anthropogenic aerosols along with ozone and Land Use and Land Cover (LULC) forcings (ANT). ; ‘historicalGHG’ the simulations of the historical climate in response to anthropogenic greenhouse gases emissions alone (GHG); ‘historicalAA’ to anthropogenic aerosols emissions alone (AA)) were only available for 7 models in the CMIP5 database (see Table S1 in Supplementary Information SI). We note here that the handling of AA and LULC forcings can greatly vary from model to model; for instance, a few models do not account for the indirect effects of aerosols (see Table S1 for more details).

3. Methods

We regridded masked all the model simulations to 1°x1° degree and masked out regions other than the Indian land region. Since the CMIP5 historical simulations ended in 2005 by experiment design, we choose the 100-year period from 1906 to 2005 for analysis, allowing us to see if the anthropogenic signal was detectable over a decade ago. The observed and model data anomalies were computed relative to climatological means over the entire period, i.e, from1906 to 2005. The CTL simulations are used to estimate the noise background against which the signals will be detected. The noise estimates are computed from CTL runs of different lengths for different models (Table S1 in SI). In order to remove potential drift behaviour in the CTL simulations of the individual models, de-drifting was done by removing a linear trend at each grid point from the anomaly time-series (computed relative to its overall time mean; Figure S1). This linear trend was removed from the corresponding historical experiments also. CMIP5;

Observed climate change is a combination of responses to external forcings (signals) and of internal climate variability (noise) along with measurement/analysis error. Isolating the signal from noise is key to D&A analysis. In order to evaluate the contribution from signal and noise in the observations, we employ the fingerprint-based D&A method described in Santer et al. (2007) - a method based on the principle that the response to each external forcing has a unique spatial pattern or "fingerprint" in the climate system (Hasselmann 1993). This method involves a search for the climate model-predicted pattern of change (the "fingerprint") in observed climate records. Our aim is to investigate whether there is a correspondence between the model-predicted fingerprint and the observational data, and then to determine whether or not such correspondence could spuriously arise from natural climate variability alone. The fingerprint corresponds to the geographical pattern that arises in response to a set of forcings, and is defined as the leading empirical orthogonal function (EOF-1) of the average of model simulations subject to those forcings (Santer et al., 2007). The associated Principal Component (PC) time-series is often associated with a long-term trend. Both model averaging and EOF calculation are effective techniques to separate the effect of long-term external forcing from the changes caused by short-term dynamics by focusing on timescale variations. We begin by comparing the trends and variability in different model simulations against the observation to evaluate whether the models are fit for carrying out the D&A analysis.

To compute the fingerprint, we first defined, for each realization, the temperature anomalies relative to the local climatological mean (after removing drift at each gridpoint over the domain) over the full period (from 1906 to 2005). We then calculated the multi-model ensemble mean (MMEM) by first averaging over individual model's realisations (for models with more than one realisation) and then averaging across models. We then compute the EOF-1of the ALL dataset's MMEM TAS anomalies as the fingerprint (denoted as $F_{raw\text{-}ALL}$) as in Santer et al. (2007). This EOF has an associated principal component (PC) time-series that indicates the time evolution of the captured mode. The use of multiple model ensembles 1) always provides a more realistic comparison to observations (at least of the mean climate and changes therein) than any individual model, and 2) damp internal climate variability more efficiently than if we use a limited number of realizations. For these reasons, using an MMEM to estimate the fingerprint of forced changes has become standard practice.

Our analyses include several steps. First, we compared the leading EOF pattern of other individual forcings ANT, GHG NAT, and AA with $F_{raw\text{-}ALL}$ whereby we determine the temperature pattern in response to all forcings and to single forcings. Second, the observed anomaly field is projected on $F_{raw\text{-}ALL}$, yielding a test statistic time series $Z_{OBS}(t)$. We then calculate the signal S(L) as the L-year trend in $Z_{OBS}(t)$ and a corresponding noise N(L) as the standard deviation of L-year unforced trends distribution. The noise estimate is obtained by pooling each of the CTL runs from the 7 individual models and is a better estimate of internal variability than that estimated from individual models. The details of estimating the noise covariance matrix and of S/N (as in Santer et al., 2007) are given in the Supplementary Text S1 and S2 respectively. Non-linear trends were calculated using the generalized additive model (GAM) by fitting a smooth spline as Scinocca et al. (2010). We estimate the mean change as in Box 2.2, Table 1 of Hartmann et al., (2013). As Figure S2 shows the linear least squares and a nonlinear trend fit to all India mean TAS values from the CRU 3,22 data set. We can see that the observations show behavior that appears to be a significant departure from the linearity over the 100-years.

The probability distribution functions(PDFs) of S/N of individual forcing can be estimated by computing the S/N of individual forcing by projecting the model realization onto fingerprint ($F_{raw\text{-}ALL}$). Thus we can attribute the observed TAS change by comparing the PDFs of the S/N ratio of individual forcing with the S/N ratio of observational data. More details of this analysis are given in sections 4.3 and 4.4.

Although we focus mainly on the annual changes in TAS, we also address changes during the individual seasons; December to February (DJF), March to May (MAM), June to August (JJA) and September to November (SON). To do this, we repeated the entire analysis described above to each individual season. The DJF season is the coldest over this region and MAM is the hottest season immediately preceding the monsoon rains. Although the monsoon season officially lasts from June to September, in this study we use the classical JJA season for our analysis.

4. Results and Discussion

4.1 Time-series and trend analysis

The time-series of spatially averaged seasonal MMEM anomaly for all the experiments and seasons (Supplementary Figure S3) shows the influence of major volcanic eruptions during the 20th century expressed as a sharp decrease in temperature in the CRU observations and in the ALL and NAT simulations. The GHG simulations show a continuous increase over the entire period while the AA simulations show a decreasing TAS after around the middle of the 20th Century.

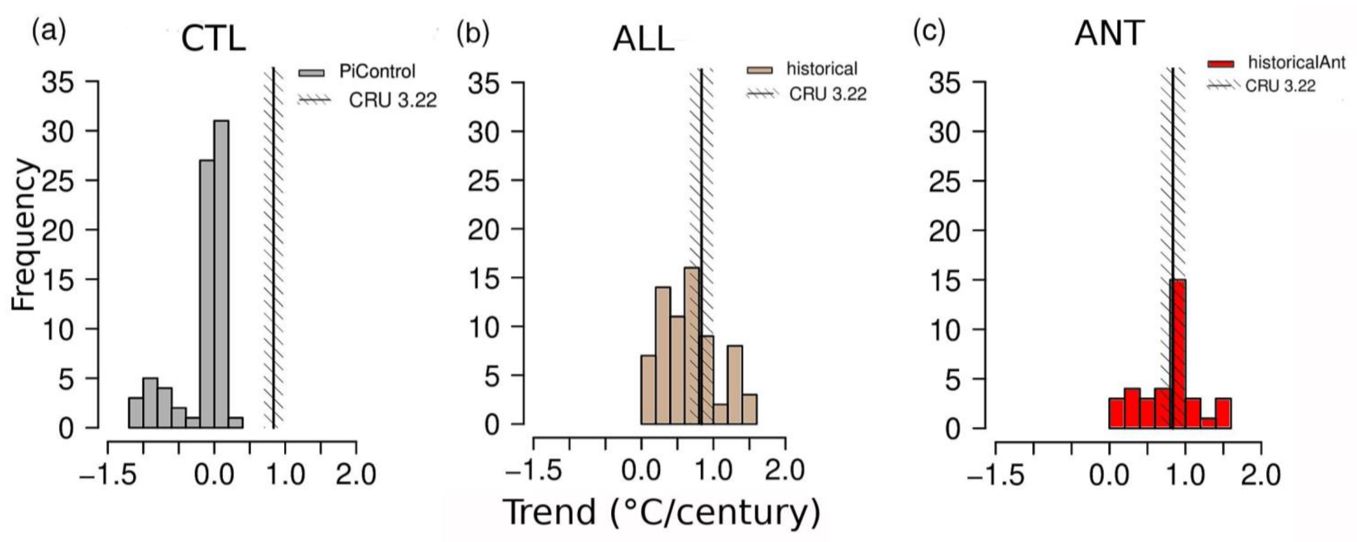

Figure 1: Comparison of observed 100-year TAS nonlinear trends (solid black line) with the distribution of 100-year TAS trends obtained from (a) the CTL simulations, (b) the ALL forcing simulations, and (c) the ANT forcing simulations. The sample distributions of unforced trends (grey bars) in (a) are calculated from 74 100-year long non-overlapping segments from the 7 CTL simulations. In (b) The distribution of ALL forcing trends (brown bars) is calculated from 70 ALL realizations. In (c) the distribution of ANT forcing trends (red bars) is estimated from 36 ANT realizations. The observed trend and all forced trends are calculated over the 1906-2005 period. The non-linear trends are estimated after Scinocca et al., (2010). The hatched pattern in the observed trend indicates ±2 Standard Error of the nonlinear trend.

We then compare the observed non-linear trend in annual mean TAS (spatially averaged over India) computed over the 1906-2005 period with the distribution of unforced trends obtained from non-overlapping 100-year segments of the CTL simulations (Figure. 1 (a)). We use all the available CTL runs from 7 models, yielding a total of 7793 years from which 74 independent 100-year samples were obtained. The control run drift was not removed before calculating the 100-year trend sampling distribution. As the figure shows, there are quite a few 100-year segments with large negative trends, which indicates that model drift might be a significant issue at least in some models. This will inflate the standard error of the distribution making it harder to reject the null hypothesis that the internal variability alone could explain the observed trend. The long-term datasets of CTL simulations can produce a better estimate of internal variability (Lutsko and Takahashi, 2018). So we can assume that these model-based noise estimates are reliable**,** it appears clearly that the observational change is too large to be compatible with unforced changes resulting from internal variability alone. In contrast, the observed TAS annual mean trend of 0.84C per century over 1906-2005 (black solid vertical line) is within the distribution of ALL forcing trends (brown bars). Similarly, the observed TAS annual mean trend is within the distribution of ANT forcing trends (red bars). This shows the influence of external forcing in the observed TAS changes. The seasonal analyses (Supplementary Figure S4) lead to similar conclusions.

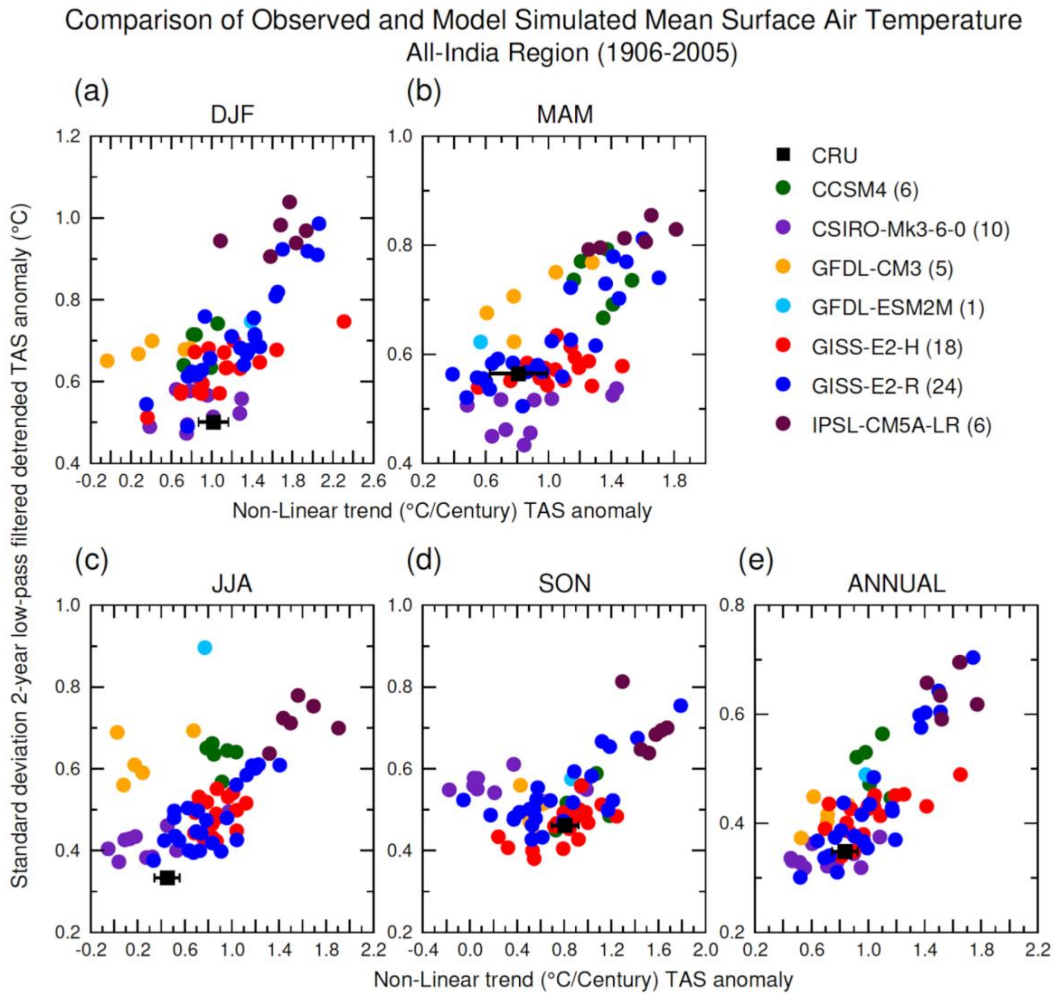

Figure 2: Comparison of observed and model simulated trend in TAS (abscissa) and standard deviation of 2-year low-pass filtered detrended TAS anomaly (ordinate) for the 1906–2005 period over India for (a) DJF, (b) MAM, (c) JJA, (d) SON, and (e) Annual averages. The trend values are computed using a non-linear spline as in Scinocca et al., (2010). The 95% confidence interval around the observed trend value (square black symbol) is represented by whiskers. Note differences in abscissa and ordinate scales across panels. In legend next to the models name, the number of ensemble members is marked within brackets.

We then compare the ALL simulations directly against the observations for the 1906-2005 period in terms of the simulated trend and low-frequency (variations below ENSO frequency) variability. In Figure 2 (a-e) we show the forced (ALL forcings simulations and observations) non-linear trends (on the x-axis) against the variability - defined as the standard deviation of 2-year lowpass filtered (using the Butterworth digital method) TAS anomaly after removing the nonlinear trend - from each for the annual and seasonal means., we compare trends, but they are clearly not linear. To capture the complex temporal behavior in the slow-varying increase in temperature over India, we prefer to use the non-linear trend rather than the linear trend. The nonlinear trend lines in observations and model ensemble members are shown in Supplementary Figure S5. The trends simulated by model ensemble members are reasonably close to the observed trend with some models [IPSL-CM5A-LR, GFDL-CM3 and GFDL-ESM2M] overestimating it in all seasons. Determining whether external factors that are responsible for temperature change over India depends on the reliability of the model-based noise estimates - which are related to a realistic simulation of internal variability. We find that models generally simulate higher than observed variability and only the GFDL-CM3 systematically underestimates variability than is observed in MAM season. Considering the shorter 50-year period of 1956-2005 (Figure S6), we can also compare the model results to a second observational dataset from the IMD. It is clearly seen that the IMD trends are consistently lower than the CRU trends with marked differences in the DJF and annual means. The IMD variability is also consistently lower than that of CRU except during the MAM and JJA seasons. Most of the models simulate larger than observed variability and trends (except in the MAM season).

The noise at a longer timescale (such as decadal scale) is not discussed here, but has been evaluated by DKA (their Figure 2a) for the same CMIP5 models and observation (CRU 3.22). A systematic model underestimation of the amplitude of TAS variability on decadal frequencies would lead to artificially low estimates of climate noise leading to spurious detection. The analysis of DKA shows that most of the models simulate larger than observed variability over both 100-years and 50-years time scales, which gives us confidence to use these CMIP5 models for a D&A analysis.

4.2 Fingerprint Identification.

In Figure 3, we display the spatial and temporal components of the $F_{raw\text{-}ALL}$ fingerprint and the leading EOF of individual forcing runs estimated separately for the annual mean case. Each EOF-1 (Figure 3 (a)) represents the expected pattern in response to the forcing in consideration, according to the models. Each EOF-1 has an associated principal component (PC) time-series (Figure 3 (b), colored lines) that indicates the time evolution of the captured mode. Each pattern is found individually and is independent of the other forcings. As expected, the model $PC_{NAT}(t)$ (green line) clearly shows the effects of volcanic eruptions on the regional temperature. While the $PC_{AA}(t)$ (blue line) shows that the cooling effect of AA is getting stronger over the observational period, the $PC_{GHG}(t)$ (red line) and $PC_{ANT}(t)$ (olive green line) show a positive trend indicating warming over the same period. These trends in PC(t) in the ALL, GHG, ANT, and AA cases show that the magnitude of the externally forced fingerprint increases with time in the simulations. Supplementary Figure S7 (a) shows the $F_{raw\text{-}ALL}$ patterns of individual seasons and the differences indicate a seasonal signature in the annual changes. We have examined individual model EOF patterns and PC time-series (not shown) and find that the MMEM captures the broad similarities across models well. Therefore, for temperature, the number of models seems enough to obtain fingerprints that are physically interpretable spatially (patterns) and temporally (PCs). We compared the correlation between the PC time series of the individual fingerprints and the time-series obtained by projecting the observations on to $F_{raw\text{-}ALL}$ patterns. The correlation with the PC time series of $F_{raw\text{-}ALL}$ is 0.698, which is higher than correlation obtained with the PC time series associated with other F_{raw} patterns (corresponding correlations for GHG, NAT, AA, and ANT PC time series are 0.66, 0.03, -0.60, and 0.64, respectively). This illustrates that the observed signal cannot be explained by noise, GHG, NAT, AA or ANT forcings alone, but is best captured in space and time by the models that include all the forcings, together.

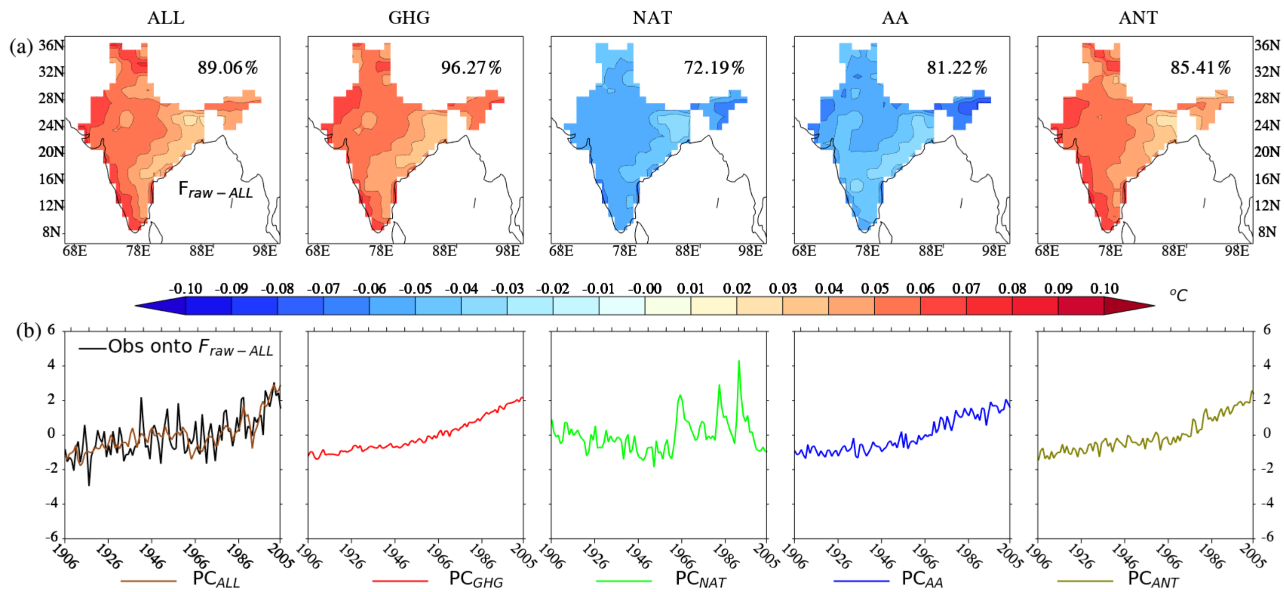

Figure 3: (a) The leading EOF of MMEM annual-mean TAS anomalies corresponding to the ALL (i.e $F_{raw\text{-}ALL}$), GHG, NAT, AA, and ANT simulations. The percentage of variability explained by the leading EOF is given in the top right corner of each panel. (b) Principal component time-series associated with the leading EOF pattern of ALL, GHG, NAT, AA and ANT patterns (colored lines). The signal time-series $Z_{OBS}(t)$ obtained by projecting the observed TAS anomalies onto $F_{raw\text{-}ALL}$ is also shown as a black line in the far left panel in (b).

4.3 Detection

We now focus on the $F_{raw\text{-}ALL}$ fingerprint. First, we show again in Figure 4 (a) the Signal time-series ($Z_{OBS}(t)$) obtained by projecting the observed onto $F_{raw\text{-}ALL}$ (as in Figure 3 (b), far left panel), along with the 100-year trend line. The positive trend in $Z_{OBS}(t)$ indicates that the expected temperature response to

$F_{raw\text{-}ALL}$ is expressed in the observations and growing through time. We then calculate the S(L)/N(L) ratio for L=100 years, where S(L) is the trend in $Z_{OBS}(t)$ over the 1906-2005 period and N(L) is the standard deviation of 100-year unforced trends distribution. To compute N(L), we first project the TAS anomalies from individual models CTL simulations onto $Z_{OBS}(t)$ to obtain Noise time-series, and we estimate, from those noise time-series, the 100-year unforced trends distribution and the standard deviation across these unforced trends. The probability density functions (PDFs) of 100-year S/N ratios for individual sets of experiments are then computed (as in Marvel and Bonfils, 2013). We display those results in Figure 4 (b): the observed S(L)/N(L) ratio is denoted by the vertical line and gray shading (to denote the trend uncertainty), while the distribution of unforced non-overlapping 100-year CTL trends is indicated in light blue. The PDF of the S/N ratio for CTL is centered around zero because there are no forcings, so there is no similarity between the CTL data and the fingerprint, except by chance. In addition to that, the observed S/N ratio is well outside the unforced distribution and above the 1% significance threshold. This implies that the observed change cannot be explained by internal variability alone. However, the PDF of S/N ratio for CTL and NAT are close because the influence of NAT forcings is less than the other external forcings (Dileepkumar et al., 2018). But the NAT and CTL PDFs are significantly different as we show in Section 4.4 . The AA is shifted more towards the left because AA forcings produce a cooling instead of the expected warming described by the fingerprint. CTL, AA, NAT, and GHG cannot explain the observation alone. Only the ALL and ANT, which include human influence, can.

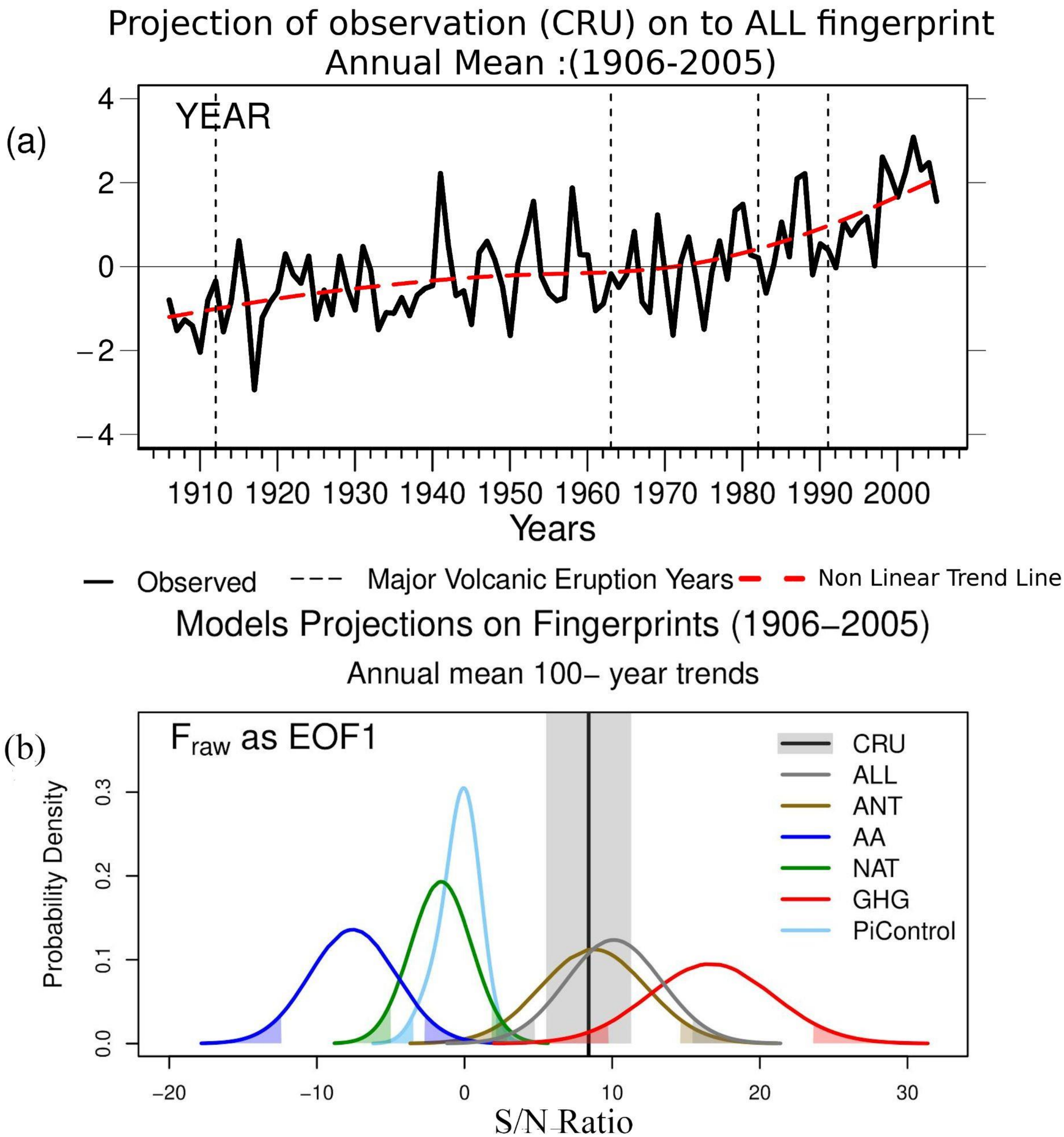

Figure 4: (a) $Z_{OBS}(t)$ time-series (solid black line) obtained by projecting the observed annual mean anomaly time series onto $F_{raw\text{-}ALL}$ along with the best-fit trend line (red dashed line). The dashed vertical lines denote the timings of major volcanic eruptions. (b) Probability distribution functions (PDFs) of best-fit 100-year trends (over 1906-2005) in the projection of model data (individual realizations) onto $F_{raw\text{-}ALL}$. All the PDFs have been normalized by the standard error of the CTL distribution N to obtain S/N ratios. The CTL, NAT, GHG, AA, ANT, and ALL distributions are displayed in light blue, green, red, blue, brown and grey, respectively. The unforced trends are calculated from the 74 non-overlapping 100-year segments from the 7,793-year concatenated $C(t)$ noise time series.

The shaded area at the tail of each PDF denotes the two-sided 90% confidence intervals. The black vertical line indicates the observed S/N ratio and the shaded grey box ±2 Standard Error of the trend. All trends are non-linear trends calculated as in Wood (2006) and Scinocca et al. (2010).

4.4. Attribution

Having detected a change, we now assess whether the observed signal is compatible with forced model simulations in order to attribute it to external forcing. To do that, we estimated the S/N ratio for each model realization of individual forcing by projecting the TAS anomaly onto $F_{raw\text{-}ALL}$ (as in Supplementary Text S2). The best-fit normal probability distribution functions (PDFs) on the S/N ratios of individual forcing realizations are shown in Figure 4(b). It is seen clearly that the observed S/N ratio is located near the mean of the ALL and ANT forcing distributions and in the tail of the GHG distribution (significant at 10%). It is also clear that the observed S/N ratio falls well outside the AA and the GHG distributions (above the 5% significance threshold), showing that the change in temperatures in observations cannot be explained by the responses to AA or GHG alone. However, the observed S/N ratio is located near the mean of ANT and ALL forced distributions and there is only a slight difference between the S/N ratio distribution of ALL and ANT simulations. These results imply that the temperature change in the observations is close to the simulated temperature changes in response to the combined effects of GHG, AA, and NAT forcings, as represented by the ALL simulations.

Because of the similarity between the NAT (green line) and CTL (cyan line) trend distributions, and the fact that these distributions (centered around zero) differ significantly from the distributions of anthropogenically forced runs, natural climate variability (which combine internal climate variability and of forced responses to natural forcings) alone is unlikely to explain the observed changes. A two-sample Kolmogorov-Smirnov test (see Table 1) reveals that the ANT and ALL trends do not differ significantly from each other, but all other pairs of distributions are significantly (at 1%) different from each other. Overall, our results indicate that the observed change in temperature over the 100-year time frame is externally forced, and requires all the forcings to be best explained. Figure 4(b) shows that the S/N ratio distribution of CTL is centered around zero, and the NAT is slightly to the left of CTL. This indicates that NAT has a slight cooling, and as shown in Table 1, NAT is significantly different from CTL. This result is consistent with the result of DKA. The S/N ratio distribution of ALL (which includes natural as well as ANT forcings) has a slight shift towards the positive side compared to ANT. However, ANT and ALL are not significantly different (Table 1).

In order to test whether using a linear trend based pattern instead of the EOF pattern as the fingerprint affects the results in any way, we repeated the analysis using the linear trend pattern (Supplementary Figure S7 b) obtained from the ALL MMEM as "raw fingerprint". We found that the S/N ratio distribution (Supplementary Figure S8) from using linear trend patterns is similar to the one using EOF patterns (compare with Figure 4) indicating that the results are robust for choice of fingerprint. This is to be expected given the close similarity between the leading EOF pattern and the linear trend pattern.

Annual Mean: $F_{raw\text{- }ALL}$						
	CTL	ANT	NAT	AA	GHG	ALL
CTL	---	R***	R***	R***	R***	R***
ANT		---	R***	R***	R***	N
NAT			---	R***	R***	R***
AA				---	R***	R***
GHG					---	R***
ALL						---

Table 1: Results of Kolmogorov-Smirnov (two sample) tests on the CMIP5 control and individual forcings runs trend distributions for annual mean. The null hypothesis is, H_0: The trends are drawn from the same distribution. We accept H_0 is if p-value>0.05.and marked as **'N'** and 'R' to denote that the null hypothesis is rejected with 90% (*), 95% (**), or 99%(***) confidence. The table shows the KS test results for the raw fingerprint patterns.

4.5 D&A for the individual seasons

We repeated the above analysis for individual seasons DJF, MAM, JJA, and SON. We found that the $F_{raw\text{-}ALL}$ patterns differ spatially across seasons (Supplementary Figure S7). The time series obtained by projecting the observed pattern on to $F_{raw\text{-}ALL}$ of DJF, MAM, JJA, and SON (Supplementary Figure S9 (a-d)) are all seen to have a positive trend clearly showing that the externally forced fingerprint is present and growing in the observations during all seasons. The PDFs of S/N ratios for DJF, MAM, JJA and SON seasons (Supplementary Figure S9 (e-h)) also show that observed S/N ratio drops well outside the AA and the GHG distributions -results similar to the case of annual mean. However, for the DJF season the kurtosis (peakedness) of S/N ratio distribution is greater than the other seasons, indicating that the winter season TAS changes are more consistent across models and realizations compared to other seasons. We repeated the two-sample Kolmogorov-Smirnov test with the PDFs of S/N ratios (Supplementary Table S2) and obtained results similar to the analysis of annual means when we consider MAM, JJA, and SON (Table S2 (b), (c), and (d)). But for the DJF season, the KS test results show that all pairs of distributions are significantly (at 1%) different from each other (Table S2 (a)).

4.6 Sensitivity of the D&A results to the choice of observations and analysis period.

Does choosing a different observational dataset affect our results? To answer this question we repeated the analysis using TAS from the IMD observational dataset available for the period 1956-2005 and compared our results with the CRU data subset for the same period. The EOF response signal estimates from model runs are also estimated from 1956-2005. Figure 5 shows the projection of IMD (solid black line) and CRU (solid red line) onto $F_{raw\text{-}ALL}$ along with the trend lines. Both lines show similar patterns and as in Figure 4(a), we can see a positive trend in the signal time-series for both IMD and CRU but with a larger trend when using the CRU dataset. The corresponding S/N ratios of IMD and CRU (denoted by vertical dashed and solid black lines) in Figure 5 (b) are similar to the values in Figure 4 (b). While both S/N ratio of CRU and IMD observations are compatible with the S/N of ANT and ALL distributions, only the S/N ratio of CRU are incompatible with the CTL and NAT distributions. Therefore, we conclude that the choice of observational dataset or analysis period has considerable influence on the detectability of the observed forcings, but not on the possible attribution of external forcings.

.

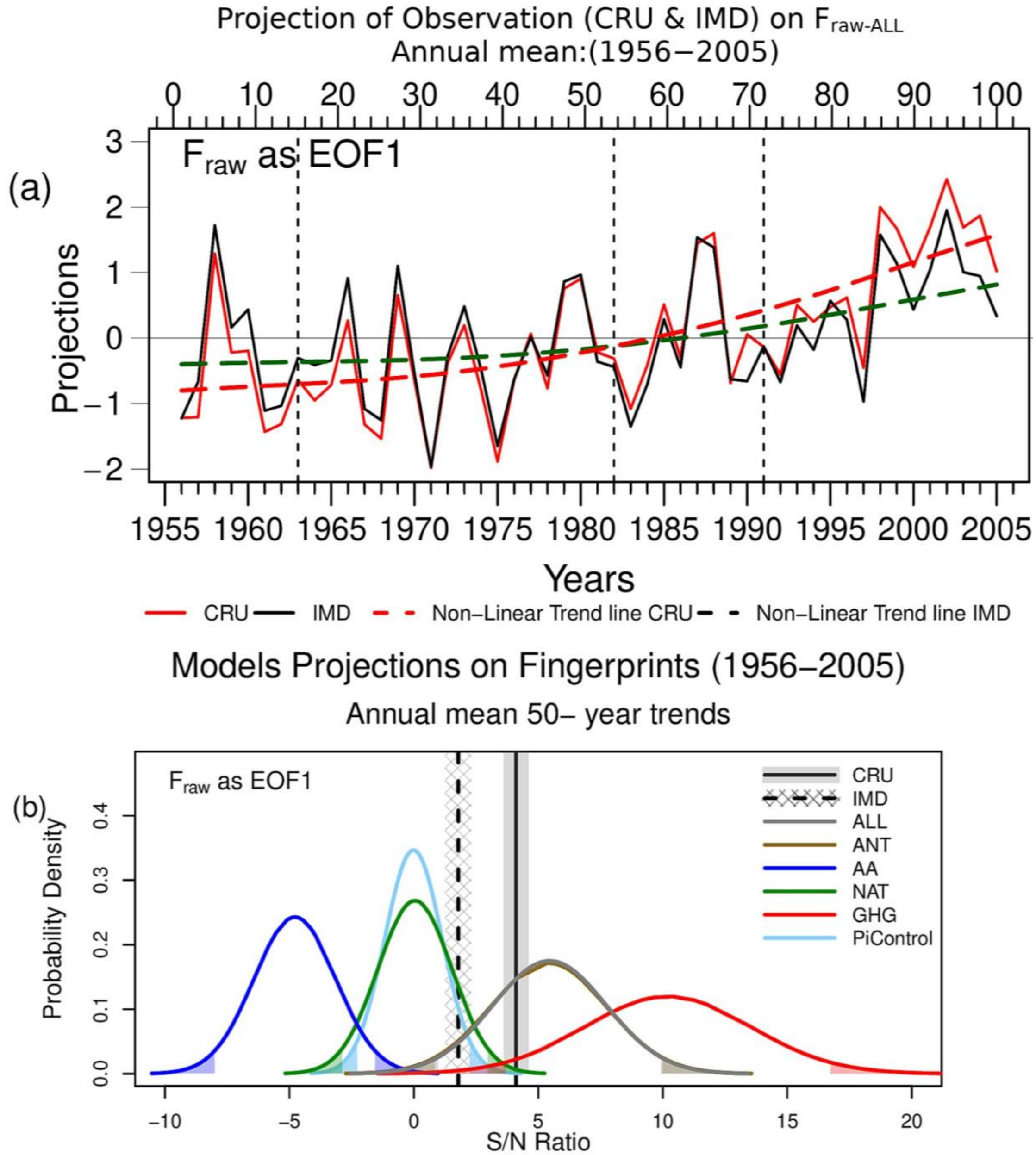

Figure 5: Same as in Figure 4, but for the 1956-2005 period with the IMD dataset (dashed vertical line) included. where the hatched pattern shows the ±2 Standard Error of IMD (calculated as in Wood, 2006; Scinocca et al., 2010).

4.7 Sensitivity of the D&A results to the choice of the number of model realizations and structural differences.

The F_{raw} patterns in Figure 3 (a) as well as S/N ratio distributions in Figure 4 (b) were estimated from MMEM using the full set of available model realizations - with different numbers of realizations for the various experiments. To check the sensitivity of D&A results to the number of model realizations, we repeated the entire analysis and estimated the $F_{raw-ALL}$ pattern from the MMEM using a set of 20 realizations that were common to all experiments (Table S1). The F_{raw} patterns using 20 realizations (Supplementary Figure S10(a)) are similar to the F_{raw} pattern using the full set of realizations (Figure 3(a)) and the S/N ratio distributions are also similar (Figure 4 and Figure S11).

To check whether positive identification of the model-predicted fingerprints is only driven by the mean increase in TAS, we conducted a test in which we removed the spatially averaged changes in TAS over India at each grid point, for each time-step and for each individual realization before repeating the entire detection analysis. In this mean-removed case, we used, again, the set of 20 realizations that were common to all experiments. The spatial structures of the F_{raw} patterns of each forcing for the “mean-removed” case (Figure S12(a)) and "mean-included" case (Figure S10(a)) cases for ALL, GHG, and ANT shows greater positive loading over the Western Himalaya region on the other hand for the fingerprint pattern for NAT, and AA shows lowest negative loading over the Western Himalaya region. The PC time-series and projected time-series (observation on to F_{raw} patterns) show an overall increasing trend for ALL, GHG, AA, and ANT in the “mean removed” and “mean-included” cases (Figure S12(b) and S10(b)). In both cases, the noise distribution is centered around zero, and the observed S/N ratio is outside the unforced distribution. However, the S/N ratio of observation is close to the mean of the distribution for ANT forcings. The observed signal being detected for the "mean-removed" and "mean-included" cases implies that the spatial structure of forced changes are distinct and are not merely caused by mean changes over the region.

5. Conclusions

We have examined the response of annual and seasonal near-surface air temperature over India to different forcings using model-derived fingerprints. Our results indicate that internal variability alone cannot explain the observed changes in surface air temperature. The model fingerprints of the response of TAS to external forcings are detectable in observations at the 1% significance level. Signals are detected in both periods (1906-2005 and 1956-2005) in CRU but not in IMD for the 1956-2005 period. Therefore the results are sensitive to the choice of observational dataset. Our analysis provides strong evidence that the increase in TAS in the annual mean and every season is primarily due to human-induced increases in GHG and partially offset by AA forcing.

Acknowledgments

We acknowledge the World Climate Research Programme’s Working Group on Coupled Modelling, which is responsible for CMIP, and we thank the climate modelling groups listed in Table S1

(Supplementary Information) for producing and making available their model output. For CMIP, the US Department of Energy's Program for Climate Model Diagnosis and Intercomparison provides coordinating support and leads the development of software infrastructure in partnership with the Global Organization for Earth System Science Portals. We thank the modelers, data processors, and those who developed and maintained the gateways at various institutions that enabled sharing the model data. The model data used in this study was obtained from http://cmip-pcmdi.llnl. gov/cmip5/ and associated CMIP5 gateways. CB was supported through the PCDMI SFA funding from the DOE Regional and Global Model Analysis Program. Work at LLNL was performed under the auspices of the U.S. Department of Energy under contract DE-AC52-456 07NA27344. We also wish to thank Dr. Benjamin D. Santer for his guidance. Authors have no conflict of interest.

Data Availability Statement

The CMIP5 dataset is available in Taylor et al. 2012 and accessible from the data portal https://esgf-node.llnl.gov/projects/esgf-llnl/. The observed CRU-3.22 mean temperature data is available in Harris et al. 2014 and available from the data portal https://crudata.uea.ac.uk/cru/data/hrg/cru_ts_3.22/. The observed IMD gridded mean temperature data is available in Srivastava et al. 2009 and obtained from the data portal http://www.imdpune.gov.in/Clim_Pred_LRF_New/Grided_Data_Download.html.

References

Attri, S. D., and Tyagi, A. (2010). Climate profile of India. *Environment Monitoring and Research Center, India Meteorology Department: New Delhi, India*.

Bindoff, N.L., P.A. Stott, K.M. AchutaRao, M.R. Allen, N. Gillett, D. Gutzler, K. Hansingo, G. Hegerl, Y. Hu, S. Jain, I.I. Mokhov, J. Overland, J. Perlwitz, R. Sebbari and X. Zhang, 2013: Detection and Attribution of Climate Change: from Global to Regional. In: Climate Change 2013: *The Physical Science Basis. Contribution of Working Group I to the Fifth Assessment Report of the Intergovernmental Panel on Climate Change* [Stocker, T.F., D. Qin, G.-K. Plattner, M. Tignor, S.K. Allen, J. Boschung, A. Nauels, Y. Xia, V. Bex and P.M. Midgley (eds.)]. Cambridge University Press, Cambridge, United Kingdom and New York, NY, USA.

Basha, G., Kishore, P., Ratnam, M. V., Jayaraman, A., Kouchak, A. A., Ouarda, T. B., and Velicogna, I. (2017). Historical and Projected Surface Temperature over India during the 20 th and 21 st century. *Scientific reports*, *7*(1), 2987.

Bonfils, C., Santer, B.D., Pierce, D.W., Hidalgo, H.G., Bala, G., Das, T., Barnett, T.P., Cayan, D.R., Doutriaux, C., Wood, A.W. and Mirin, A. (2008a). Detection and attribution of temperature changes in the mountainous western United States. *Journal of Climate*, *21*(23), 6404-6424.

Bonfils, C., Duffy, P. B., Santer, B. D., Wigley, T. M., Lobell, D. B., Phillips, T. J., and Doutriaux, C. (2008b). Identification of external influences on temperatures in California. *Climatic Change*, *87*(1), 43-55.

Dileepkumar, R., AchutaRao, K., and Arulalan, T. (2018). Human influence on sub-regional surface air temperature change over India. *Scientific reports*, *8*(1), 8967.

Gray, J. M., Frolking, S., Kort, E. A., Ray, D. K., Kucharik, C. J., Ramankutty, N., and Friedl, M. A. (2014). Direct human influence on atmospheric CO2 seasonality from increased cropland productivity. Nature 515, 398.

Harris, I. P. D. J., Jones, P. D., Osborn, T. J., and Lister, D. H. (2014). Updated high-resolution grids of monthly climatic observations–the CRU TS3. 10 Dataset. *International Journal of Climatology*, *34*(3), 623-642.

Hartmann, D.L., A.M.G. Klein Tank, M. Rusticucci, L.V. Alexander, S. Brönnimann, Y. Charabi, F.J. Dentener, E.J. Dlugokencky, D.R. Easterling, A. Kaplan, B.J. Soden, P.W. Thorne, M. Wild and P.M. Zhai, 2013: Observations: Atmosphere and Surface. *In: Climate Change 2013: The Physical Science Basis. Contribution of Working Group I to the Fifth Assessment Report of the Intergovernmental Panel on Climate Change* [Stocker, T.F., D. Qin, G.-K. Plattner, M. Tignor, S.K. Allen, J. Boschung, A. Nauels, Y. Xia, V. Bex and P.M. Midgley (eds.)]. Cambridge University Press, Cambridge, United Kingdom and New York, NY, USA.

Hasselmann, K. (1993). Optimal fingerprints for the detection of time-dependent climate change. *Journal of Climate*, *6*(10), 1957-1971.

Henson, S. A., Cole, H. S., Hopkins, J., Martin, A. P., and Yool, A. (2018). Detection of climate change-driven trends in phytoplankton phenology. Glob. Chang. Biol. 24, e101–e111. 1 doi:10.1111/gcb.13886.

Jones, G. S., Christidis, N., & Stott, P. A. (2011). Detecting the influence of fossil fuel and bio-fuel black carbon aerosols on near surface temperature changes. *Atmospheric Chemistry and Physics*, *11*(2), 799-816.

Jones, G. S., Stott, P. A., and Christidis, N. (2013). Attribution of observed historical near–surface temperature variations to anthropogenic and natural causes using CMIP5 simulations. *Journal of Geophysical Research: Atmospheres*, *118*(10), 4001-4024.

Kothawale, D. R., and Rupa Kumar, K. (2005). On the recent changes in surface temperature trends over India. *Geophysical Research Letters*, *32*(18).

Lutsko, N. J., and Takahashi, K. (2018). What can the internal variability of cmip5 models tell us about their climate sensitivity?. *Journal of Climate*, *31*(13), 5051-5069.

Marvel, K., and Bonfils, C. (2013). Identifying external influences on global precipitation. *Proceedings of the National Academy of Sciences*, *110*(48), 19301-19306.

Marvel, K., Schmidt, G. A., Shindell, D., Bonfils, C., LeGrande, A. N., Nazarenko, L., and Tsigaridis, K. (2015). Do responses to different anthropogenic forcings add linearly in climate models? *Environmental Research Letters*, *10*(10), 104010.

Mazzocchi, F., & Pasini, A. (2017). Climate model pluralism beyond dynamical ensembles. *Wiley Interdisciplinary Reviews: Climate Change*, *8*(6), e477.

Mueller, B. L., Gillett, N. P., Monahan, A. H., and Zwiers, F. W. (2018). Attribution of Arctic Sea Ice Decline from 1953 to 2012 to Influences from Natural, Greenhouse Gas, and Anthropogenic Aerosol Forcing. *J. Clim.* 31, 7771–7787. doi:10.1175/JCLI-D-17-0552.1.

Pasini, A. and Modugno, G.. (2013). Climatic attribution at the regional scale: a case study on the role of circulation patterns and external forcings. *Atmospheric Science Letters*, *14*(4), 301-305.

Pasini, A., Racca, P., Amendola, S., Cartocci, G., & Cassardo, C. (2017). Attribution of recent temperature behaviour reassessed by a neural-network method. *Scientific reports*, *7*(1), 1-10.

Santer, B.D., Mears, C., Wentz, F.J., Taylor, K.E., Gleckler, P.J., Wigley, T.M.L., Barnett, T.P., Boyle, J.S., Brüggemann, W., Gillett, N.P. and Klein, S.A. (2007). Identification of human-induced changes in atmospheric moisture content. *Proceedings of the National Academy of Sciences*, *104*(39), 15248-15253.

Santer, B.D., Painter, J.F., Mears, C.A., Doutriaux, C., Caldwell, P., Arblaster, J.M., Cameron-Smith, P.J., Gillett, N.P., Gleckler, P.J., Lanzante, J. and Perlwitz, J. (2013). Identifying human influences on atmospheric temperature. *Proceedings of the National Academy of Sciences*, *110*(1), 26-33.

Santer, B.D., Po-Chedley, S., Zelinka, M.D., Cvijanovic, I., Bonfils, C., Durack, P.J., Fu, Q., Kiehl, J., Mears, C., Painter, J. and Pallotta, G. (2018). Human influence on the seasonal cycle of tropospheric temperature. *Science*, *361*(6399), eaas8806.

Scinocca, J. F., Stephenson, D. B., Bailey, T. C., and Austin, J. (2010). Estimates of past and future ozone trends from multimodel simulations using a flexible smoothing spline methodology. *Journal of Geophysical Research: Atmospheres*, *115*(D3).

Shiogama, H. , Stone, D. A., Nagashima, T. , Nozawa, T. and Emori, S. (2013), On the linear additivity of climate forcing-response relationships at global and continental scales. Int. J. Climatol., 33: 2542-2550. doi:10.1002/joc.3607

Slangen, A. B. A., Church, J. A., Agosta, C., Fettweis, X., Marzeion, B., and Richter, K. (2016). Anthropogenic forcing dominates global mean sea-level rise since 1970. Nat. Clim. Chang. 6, 701–705. doi:10.1038/nclimate2991.

Sonali, P. and D. Nagesh Kumar. 2016. 'Detection and Attribution of Seasonal Temperature Changes in India with Climate Models in the CMIP5 Archive', Journal of Water and Climate Change, 7(1): 83–102.

Srivastava, A. K., Rajeevan, M., and Kshirsagar, S. R. (2009). Development of a high resolution daily gridded temperature data set (1969–2005) for the Indian region. *Atmospheric Science Letters*, *10*(4), 249-254.

Srivastava, A. K., Kothawale, D. R., and Rajeevan, M. N. (2017). Variability and long-term changes in surface air temperatures over the indian subcontinent. In *Observed climate variability and change over the*

Indian region (pp. 17-35). Springer, Singapore.

Stott, P. A., Tett, S. F. B., Jones, G. S., Allen, M. R., Mitchell, J. F. B., and Jenkins, G. J. (2000). External control of 20th century temperature by natural and anthropogenic forcings. *Science*, *290*(5499), 2133-2137.

Stott, P. A., Tett, S. F., Jones, G. S., Allen, M. R., Ingram, W. J., and Mitchell, J. F. (2001). Attribution of twentieth century temperature change to natural and anthropogenic causes. *Climate Dynamics*, *17*(1), 1-21.

Taylor, K. E., Stouffer, R. J., and Meehl, G. A. (2012). An overview of CMIP5 and the experiment design. *Bulletin of the American Meteorological Society*, *93*(4), 485-498.

Tett, S.F., Jones, G.S., Stott, P.A., Hill, D.C., Mitchell, J.F., Allen, M.R., Ingram, W.J., Johns, T.C., Johnson, C.E., Jones, A. and Roberts, D.L.(2002). Estimation of natural and anthropogenic contributions to twentieth century temperature change. *Journal of Geophysical Research: Atmospheres*, *107*(D16).

Tett, S. F., Stott, P. A., Allen, M. R., Ingram, W. J., and Mitchell, J. F. (1999). Causes of twentieth-century temperature change near the Earth's surface. *Nature*, *399*(6736), 569.

Triacca, U., Attanasio, A., & Pasini, A. (2013). Anthropogenic global warming hypothesis: testing its robustness by Granger causality analysis. *Environmetrics*, *24*(4), 260-268.

Undorf, S., Polson, D., Bollasina, M. A., Ming, Y., Schurer, A., and Hegerl, G. C. (2018). Detectable Impact of Local and Remote Anthropogenic Aerosols on the 20th Century Changes of West African and South Asian Monsoon Precipitation. J. Geophys. Res. Atmos. 123, 4871–4889. doi:10.1029/2017JD027711.

Wood, S. N. *Generalized Additive Models: An Introduction with R.* CRC/Chapman & Hall, Boca Raton, FL, USA, 2006

Zhou, J., and Tung, K. K. (2013). Deducing multidecadal anthropogenic global warming trends using multiple regression analysis. *Journal of the Atmospheric Sciences*, *70*(1), 3-8.

Supplementary Text for

On the emergence of human influence on surface air temperature changes over India.

Dileepkumar R.[1], Krishna AchutaRao[1], Céline Bonfils[2], Arulalan T. [1,3]

[1] *Department of Mathematics, KSMDB College, Sasthamcotta, Kerala*

[2]*Centre for Atmospheric Sciences, Indian Institute of Technology Delhi*

[3] *Lawrence Livermore National Laboratory*

[4] *India Meteorological Department, Ministry of Earth Sciences, Government of India*

Contents of this file

Text S1. Noise Data Sets

The fingerprint analysis typically needs independent data sets for estimating the background noise of natural internal variability. This set of data is needed to derive the statistical significance of the results. So, we created noise dataset C by concatenating the TAS anomaly (annual or for individual seasons) data from the preindustrial control simulations of seven models (see Supplementary Table S1 for details). The temperature anomalies used to generate C are defined relative to the local climatology over the entire period. We detrended (at each grid point) the control simulations to remove model climate drift before concatenating the anomalies from different models; Figures S1 (a) and (b) show the spatially averaged time series from concatenated piControl simulations without and with detrending, respectively. There are a total of 7793 years of piControl data in C.

Text S2. Estimation of Signal-to-noise (S/N) ratio.

The observed temperature anomalies (OBS) are projected onto the fingerprint F, the time-invariant fingerprint, to yield the signal time series $Z_{OBS}(t)$. This provides information on the fingerprint strength in the observations. If observed patterns of TAS change have become increasingly similar to F, $Z_{OBS}(t)$ would increase over time. In order to assess the significance of the changes in the signal $Z_{OBS}(t)$ we compare trends in $Z_{OBS}(t)$ with a null distribution of trends - a record in which we know a priori that any expression of the fingerprint is merely by chance. In order to estimate the noise, we use noise matrix C (see Text S1 above for details).

The noise time-series N(t) is the projection of C onto the fingerprint F. We create a distribution of L-year trends from non-overlapping L-year segments of N(t) and designate the standard deviation (∈) of these trends as the noise for trend length L. Then the S/N ratio can be derived by dividing the trend in $Z_{OBS}(t)$ by ∈.

Supplementary Tables for

On the emergence of human influence on surface air temperature changes over India.

Dileepkumar R.[1], Krishna AchutaRao[1], Céline Bonfils[2], Arulalan T. [1,3]

[1] *Department of Mathematics, KSMDB College, Sasthamcotta, Kerala*

[2] *Centre for Atmospheric Sciences, Indian Institute of Technology Delhi*

[3] *Lawrence Livermore National Laboratory*

[4] *India Meteorological Department, Ministry of Earth Sciences, Government of India*

Contents of this file

Sl No	Model	Horizontal Resolution	Number of Realizations					Total Length of piControl Runs (Years)	Forcing Factors Included in historical Experiments		
			historical	historicalGHG	historicalNat	historicalAnt	historicalAA		Sulphate Indirect	Carbonaceous Aerosols	Land use Change
1	IPSL-CM5A-LR	1.89x3.75	6	6	3	3	1	1000	Y	Y	Y
2	GFDL-CM3	2x2.5	5	3	3	3	3	500	Y	Y	Y
3	GFDL-ESM2M	1.51x2.5	1	1	1	1	1	500	**N**	Y	Y
4	GISS-E2-H	2x2.5	18	5	10	10	5	1842	Y	Y	Y
5	GISS-E2-R	2x2.5	24	5	10	10	5	3175	Y	Y	Y
6	CCSM4	0.94x1.25	6	2	1	4	3	276	**N**	Y	Y
7	CSIRO-Mk3-6-0	1.84x1.87	10	5	5	5	4	500	Y	Y	N
Total			**70**	**27**	**33**	**36**	**22**	**7793**			

Table S1: CMIP5 models used in fingerprint analysis: Model names, their institution names, data resolution, number of initial condition ensemble members for each experiment, and number of years available for each model's pre-industrial control run (including the realizations) also listed. The last column shows the forcing factor accounted for in addition to the model runs. Y indicates factor included and N indicates factor not included.

(a)

DJF: $F_{raw-ALL}$						
	CTL	ANT	NAT	AA	GHG	ALL
CTL	---	R***	R***	R***	R***	R***
ANT		---	R***	R***	R***	R***
NAT			---	R***	R***	R***
AA				---	R***	R***
GHG					---	R***
ALL						---

(b)

MAM: $F_{raw-ALL}$						
	CTL	ANT	NAT	AA	GHG	ALL
CTL	---	R***	R***	R***	R***	R***
ANT		---	R***	R***	R***	N
NAT			---	R***	R***	R***
AA				---	R***	R***
GHG					---	R***
ALL						---

(c)

JJA: $F_{raw-ALL}$						
	CTL	ANT	NAT	AA	GHG	ALL
CTL	---	R***	R***	R***	R***	R***
ANT		---	R***	R***	R***	N
NAT			---	R***	R***	R***
AA				---	R***	R***
GHG					---	R***
ALL						---

(d)

SON: $F_{raw-ALL}$						
	CTL	ANT	NAT	AA	GHG	ALL
CTL	---	R***	R***	R***	R***	R***
ANT		---	R***	R***	R***	N
NAT			---	R***	R***	R***
AA				---	R***	R***
GHG					---	R***
ALL						---

Table S2: As in Table 1 (main text), but for (a)DJF season (b) MAM, (c) JJA and (d) SON season respectively.

Supplementary Figures for

On the emergence of human influence on surface air temperature changes over India.

Dileepkumar R.[1], Krishna AchutaRao[1], Céline Bonfils[2], Arulalan T. [1,3]

[1] *Department of Mathematics, KSMDB College, Sasthamcotta, Kerala*

[2] *Centre for Atmospheric Sciences, Indian Institute of Technology Delhi*

[3] *Lawrence Livermore National Laboratory*

[4]*India Meteorological Department, Ministry of Earth Sciences, Government of India*

Contents of this file

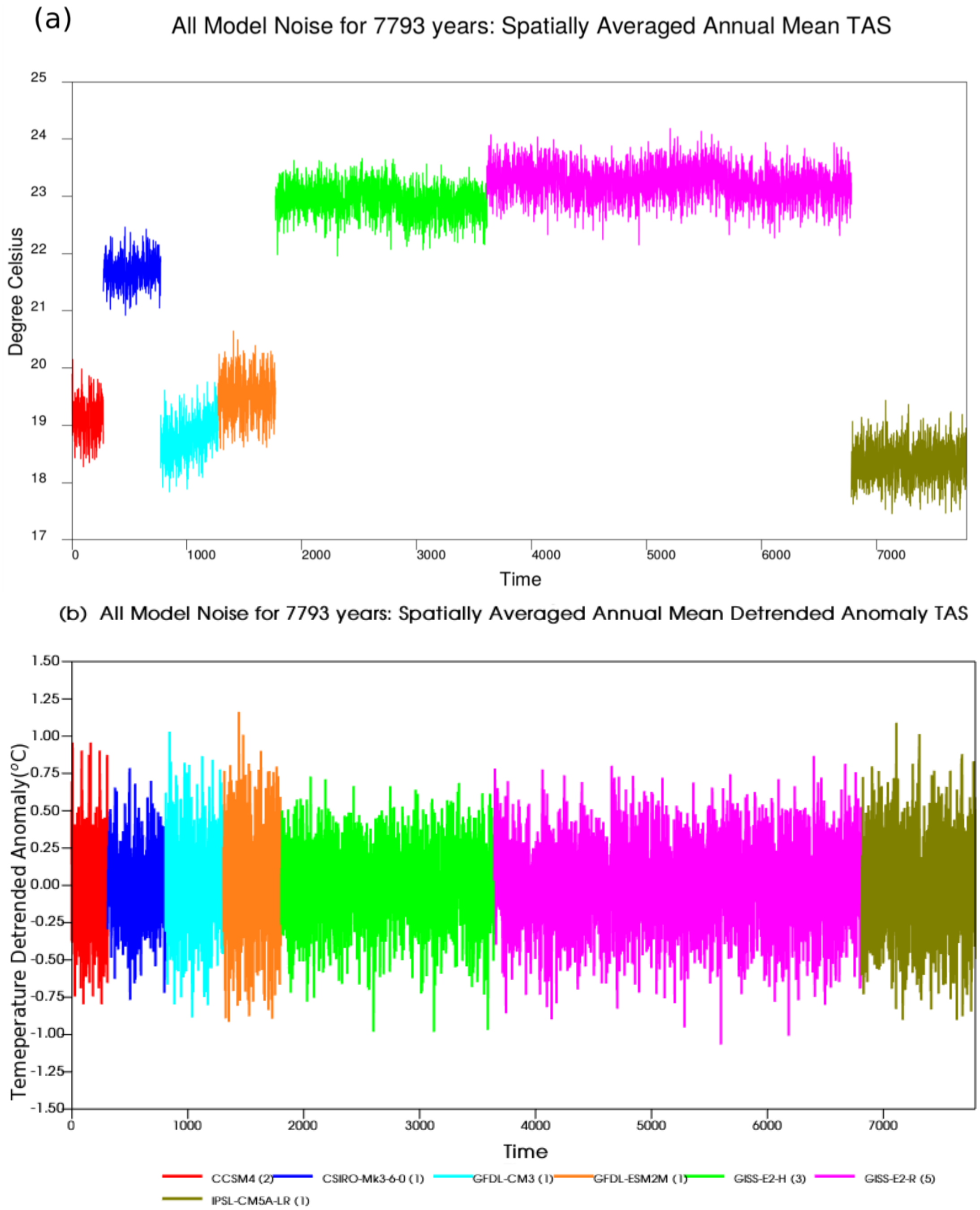

Figure S1: Annual-mean TAS spatially averaged over the Indian continental region from 7 CMIP5 models before (a) and after (b) detrending. The number in brackets next to the model names indicates the number of CTL realizations.

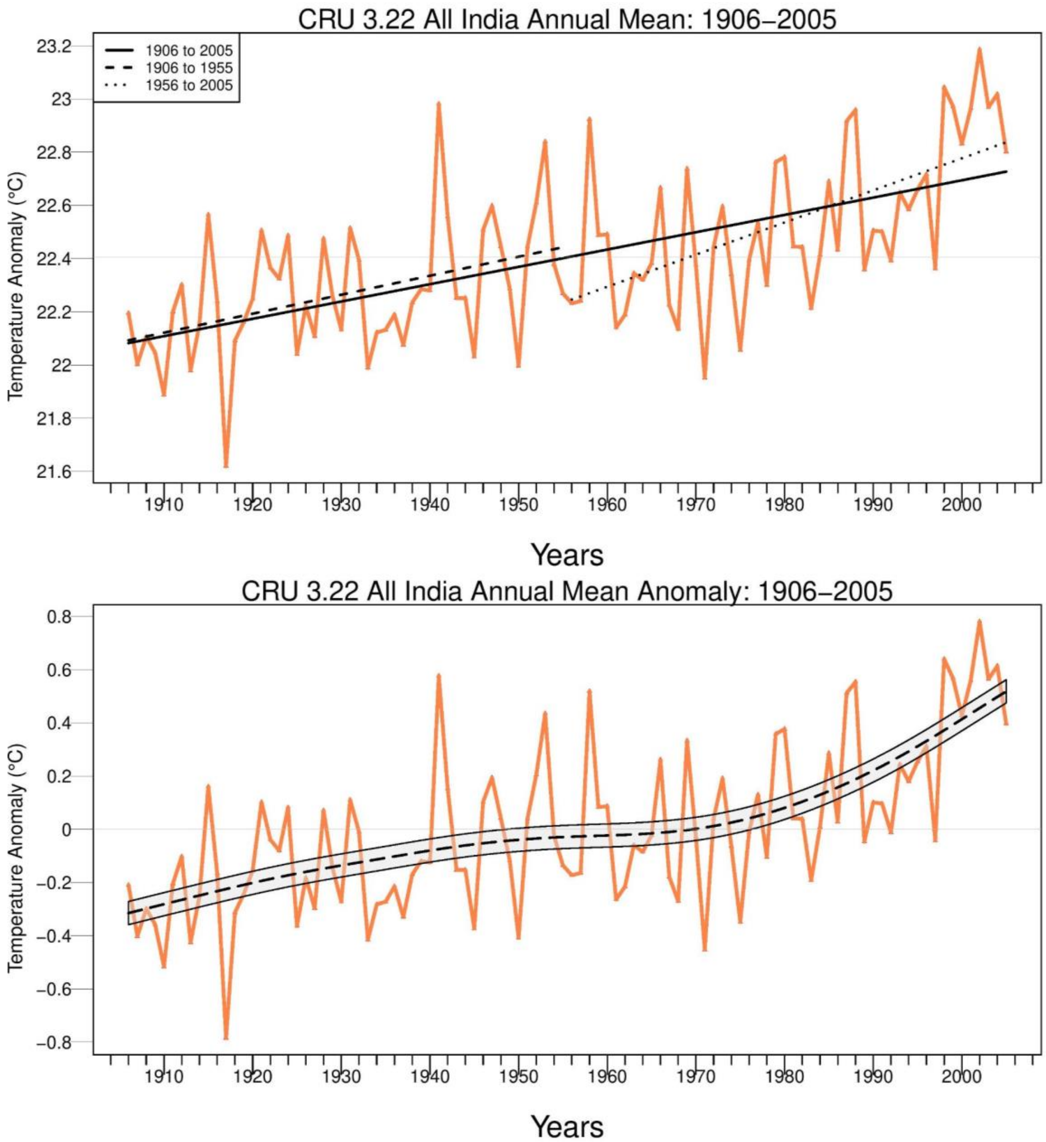

Figure S2: (a) All India mean TAS anomalies for 1906-2005 relative to full-time period climatology based on CRU 3.22 annual data. The straight black lines are the least-squares trends for 1906–2005 (solid), 1906–1955(dashed), and 1956–2005 (dotted). (b) Same data as in (a), with smoothing spline (dashed curve) using Generalized Additive Model and the ±2 Standard Error shown as gray shading on the smooth curve.

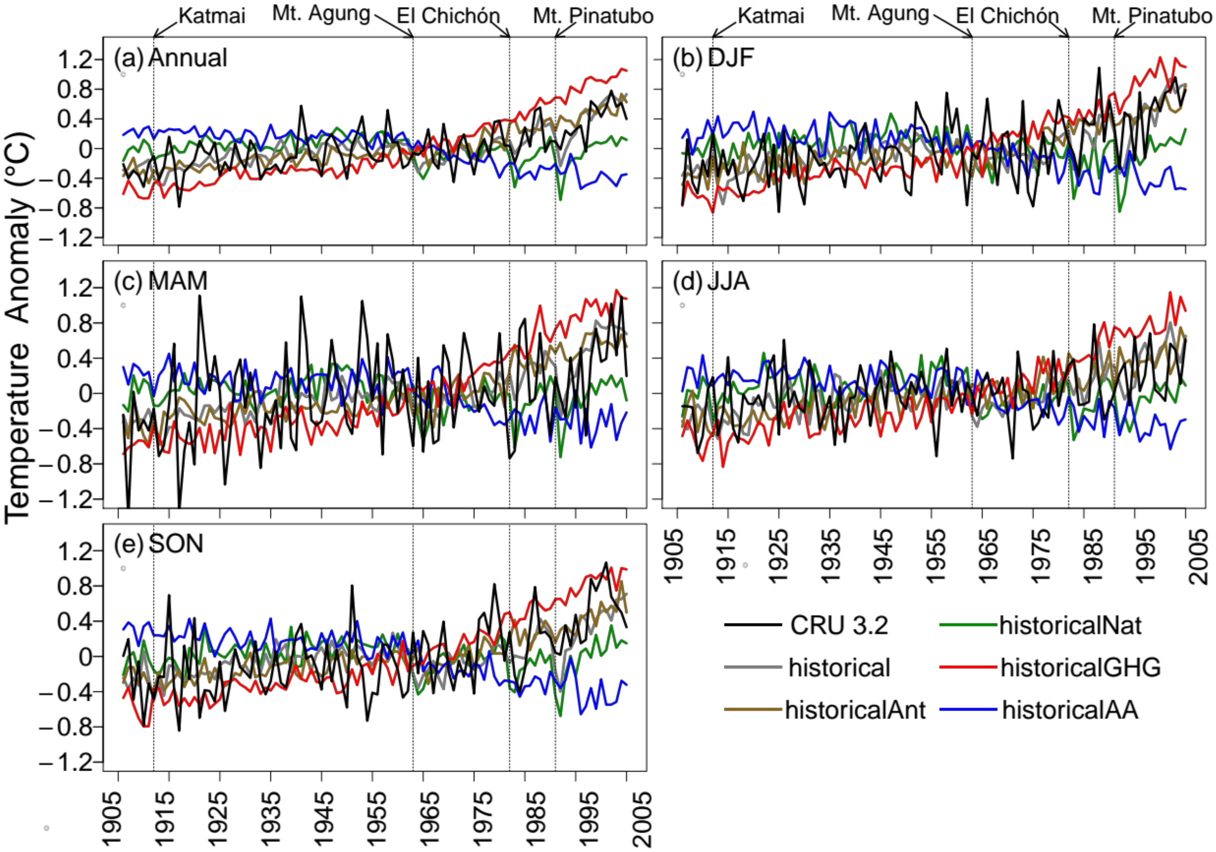

Figure S3: (a) Observed and simulated annual Mean Temperature Anomaly (relative to the 1906–2005 average period). Results are shown for CRU 3.2 (black), and the MMEM of ALL (grey) NAT (green), ANT (brown), GHG (red), and AA (blue) simulations for Indian land region. (b), (c), (d), and (e) is the same as (a), but for DJF, MAM, JJA, and SON seasons, respectively. The dotted vertical lines in panels show timings of major volcanic eruptions during the 1906–2005 period.

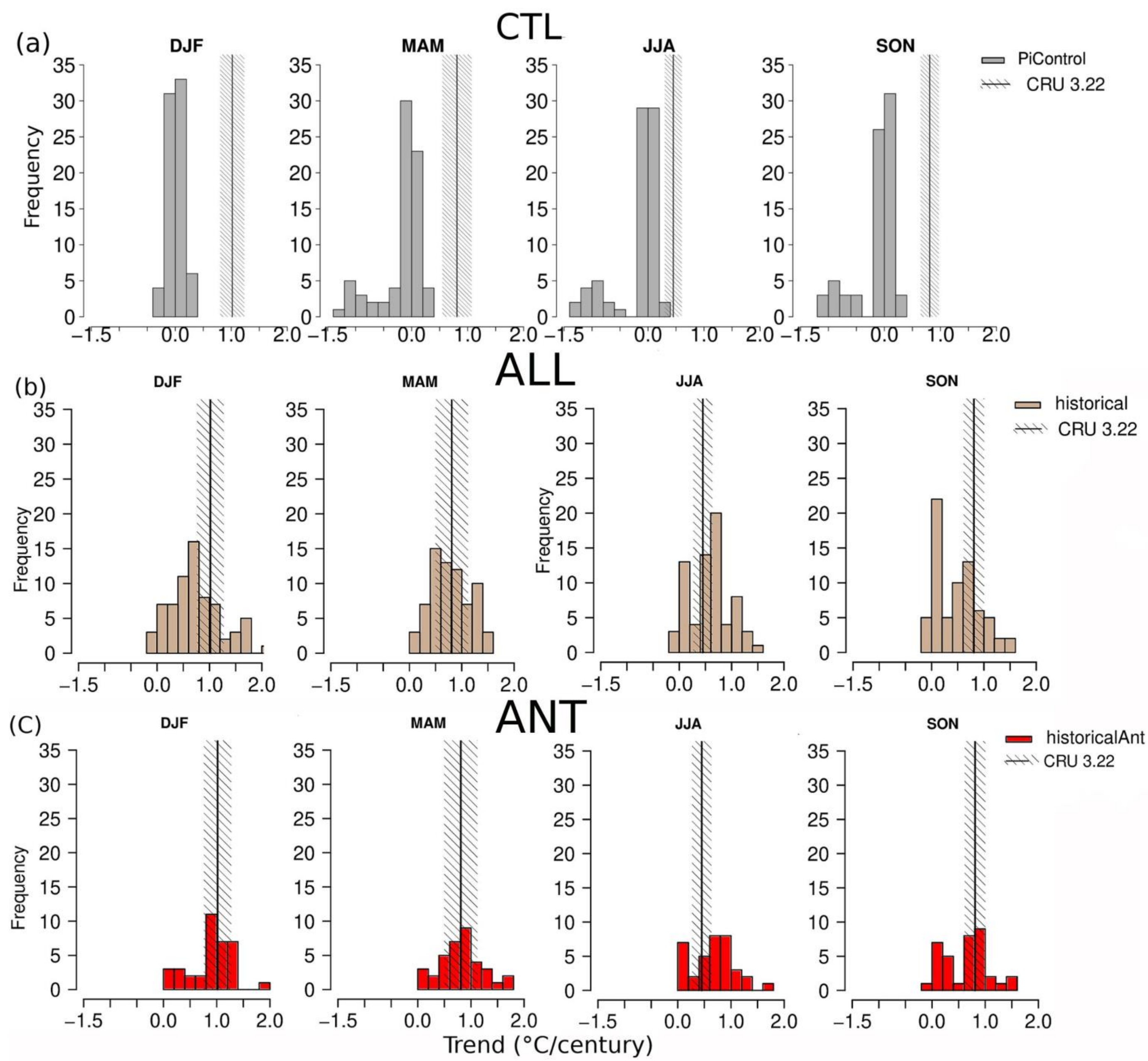

Figure S4: (a) CTL results as Figure 1(a), but for the DJF, MAM, JJA, and SON seasons, respectively (from left to right). Rows (b) and (c) as (a) but for ALL and ANT forcing simulations respectively.

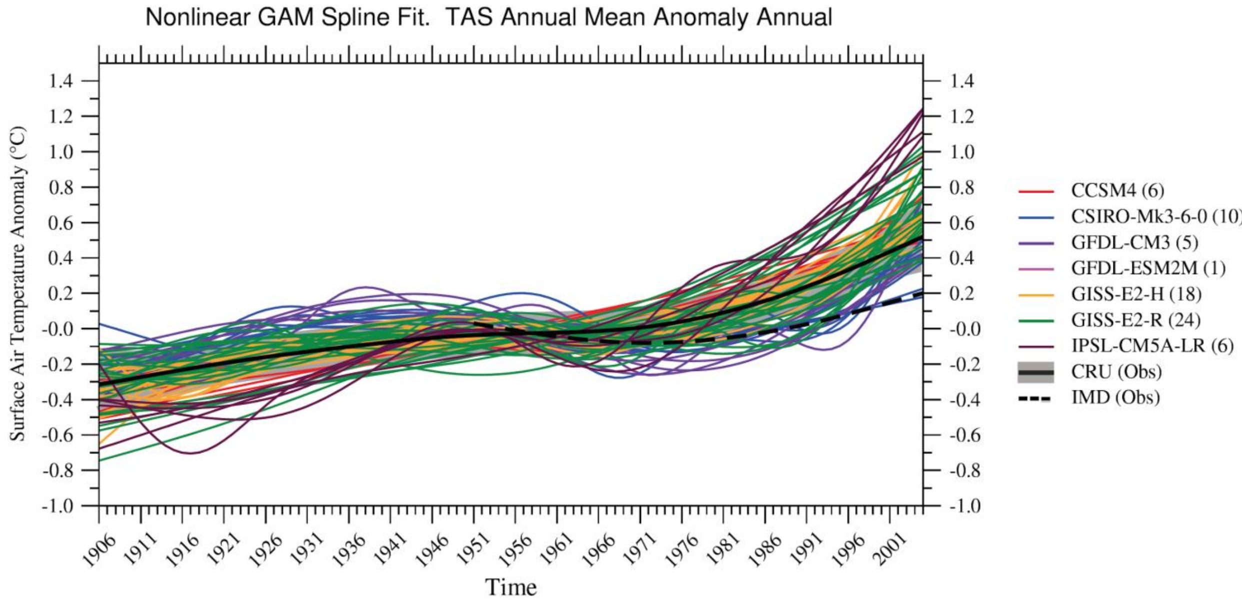

Figure S5: Nonlinear GAM spline fit to observed and simulated (ALL forcings) annually-averaged TAS over India for the 1906–2005 period. The CRU observed trend (black solid line) and its 95% confidence intervals (light grey shade); IMD observed trend (black dashed line) estimated as in Scinocca et al., (2010) and Wood (2006).

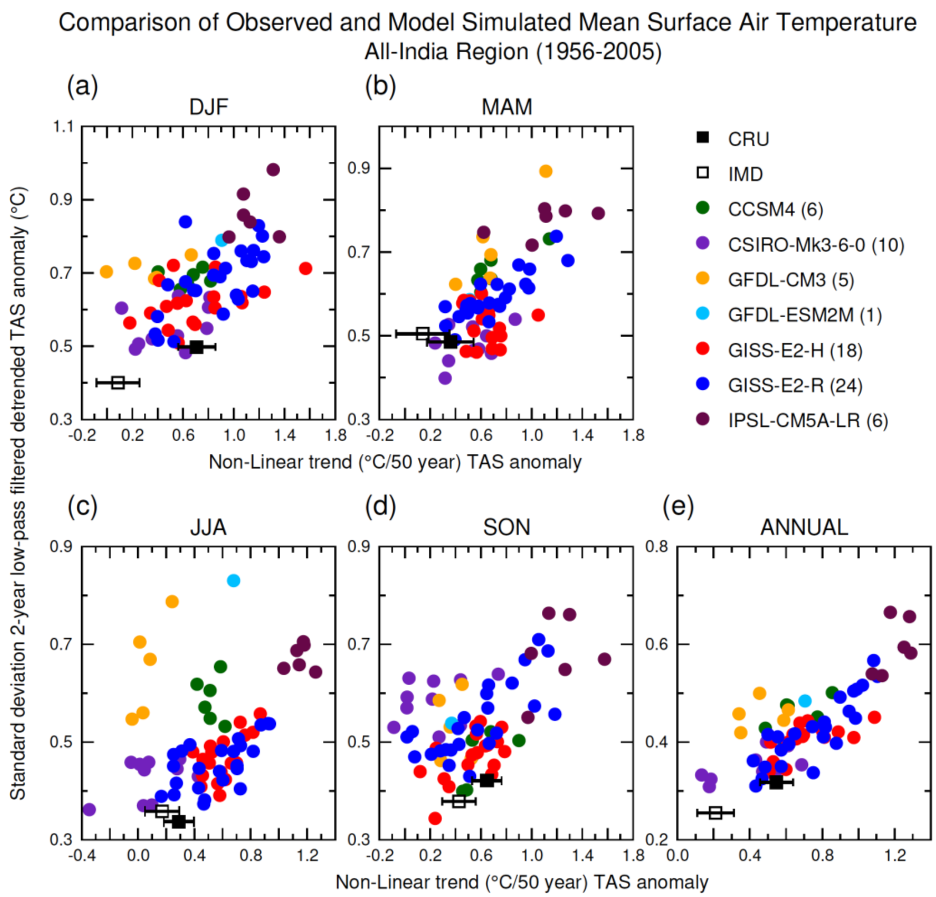

Figure S6: Same as Figure 2 in the main text but for the 1956-2005 period (50 years). The IMD observation is added and denoted in white square symbol. Note differences in abscissa and ordinate scales across panels. In legend next to the models name, the number of ensemble members is marked within brackets.

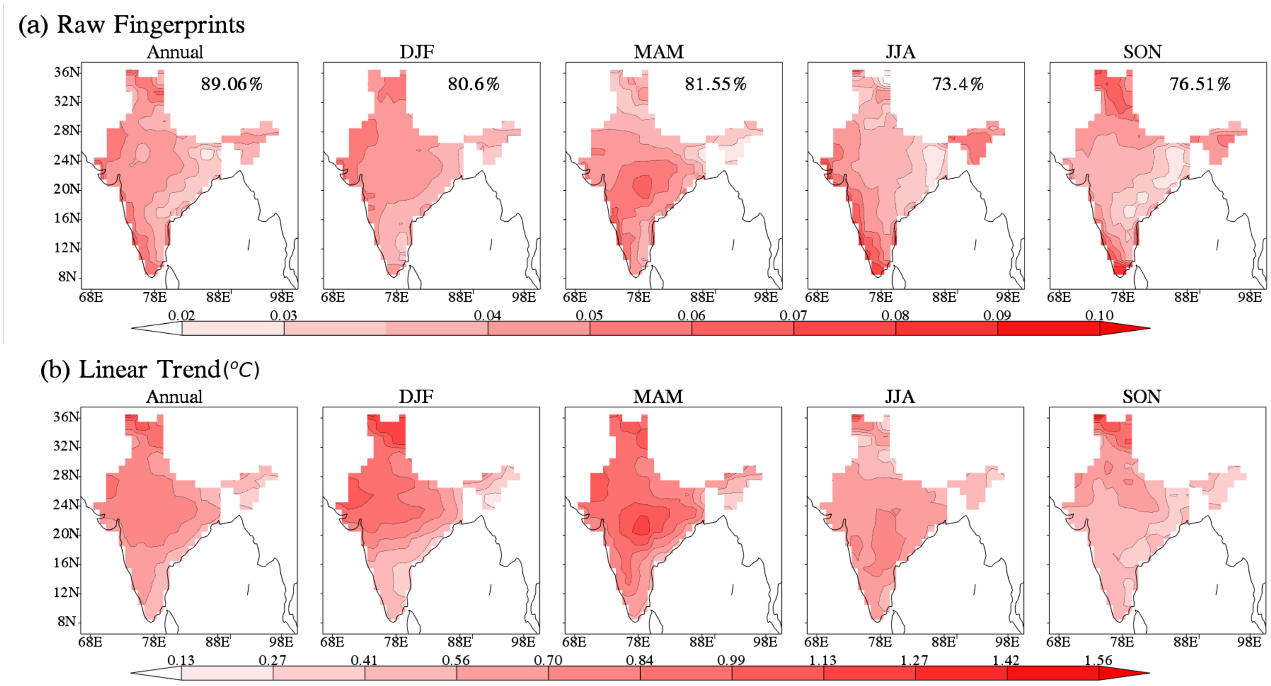

Figure S7: (a) Raw fingerprints ($F_{raw\text{-}ALL}$) for the annual mean and DJF, MAM, JJA, and SON seasons of TAS anomaly for the 1906-2005 period. The percentage of variability explained by the leading EOF is given in the top right corner of each panel. (b) The 100-year linear trend of annual mean, DJF, MAM, JJA, and SON TAS anomalies respectively.

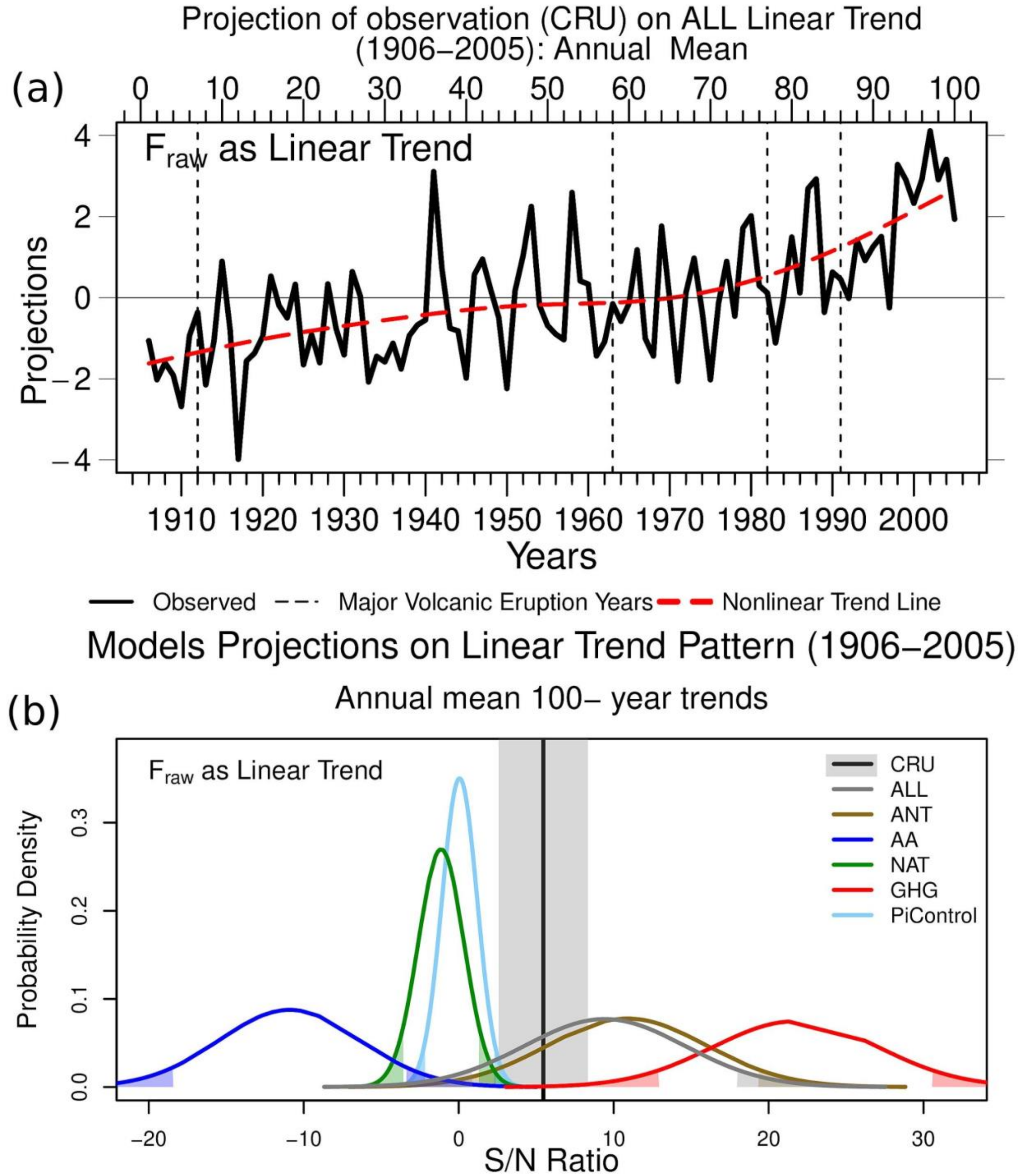

Figure S8: Same as Figure 4 in the main text, but using the linear trend pattern as the fingerprint.

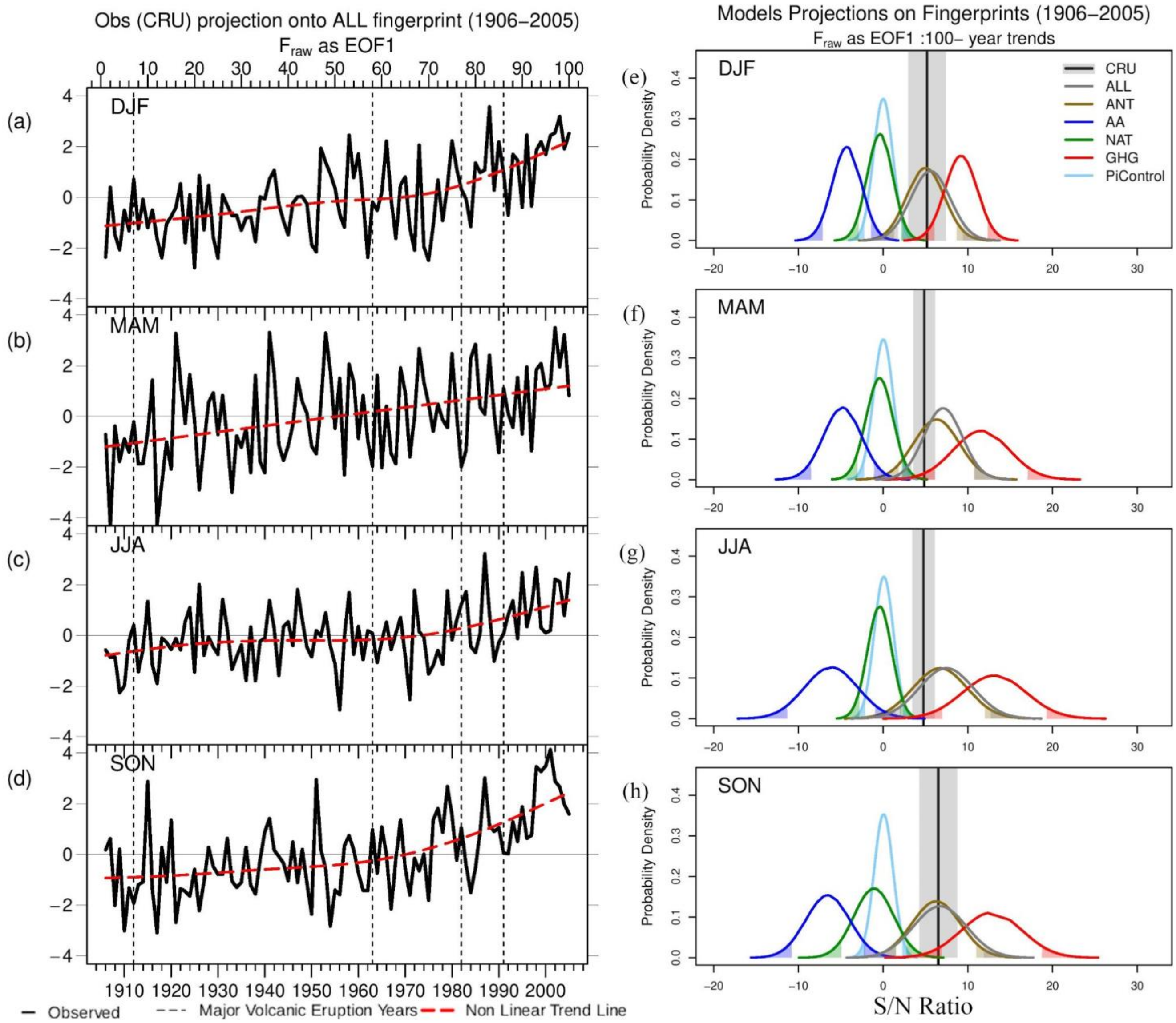

Figure S9: Same as Figure 4 (main text) but for DJF season(panels a, e), MAM (panels b, f), JJA (panels c, g), and SON (panels d, h) seasons respectively.

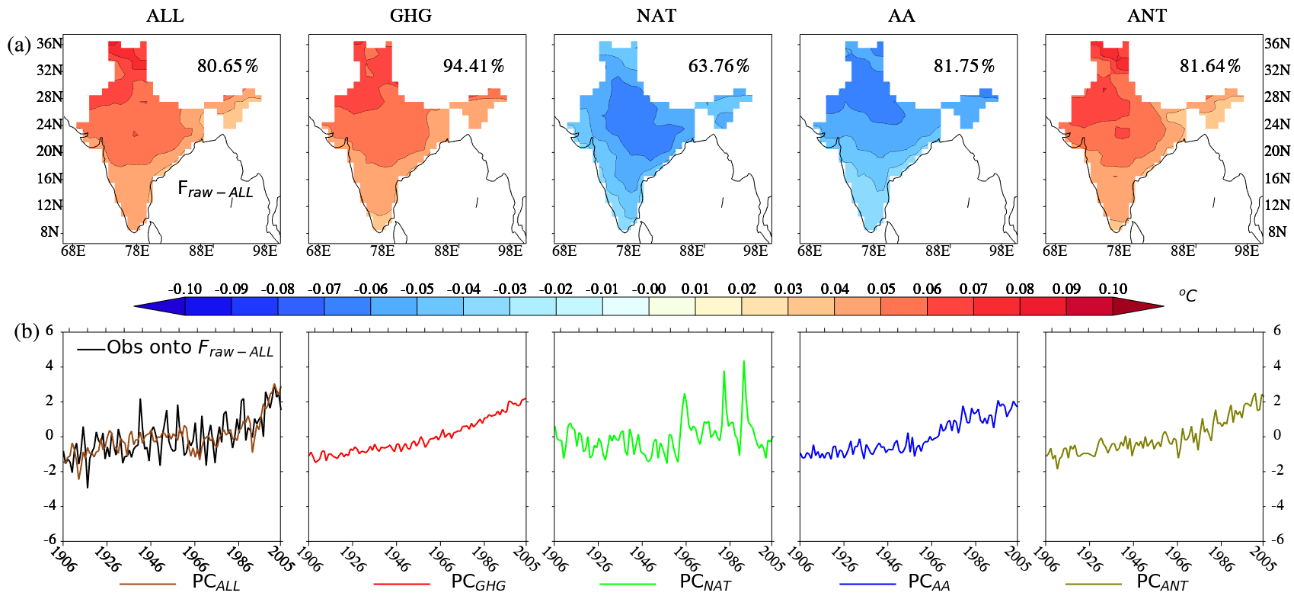

Figure S10: Same as Figure 3 but using the 20 realizations common to all the forcing experiments.

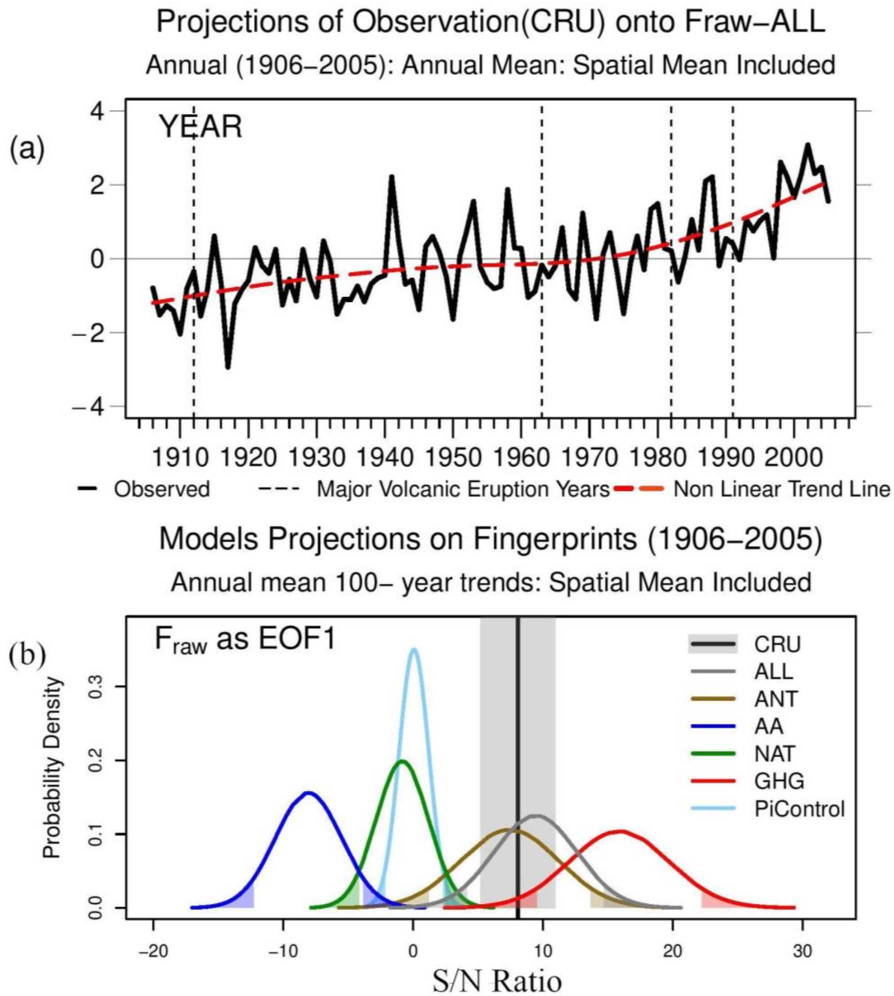

Figure S11: Same as Figure 4 in the main text, but using the 20 realizations common to all the forcing experiments.

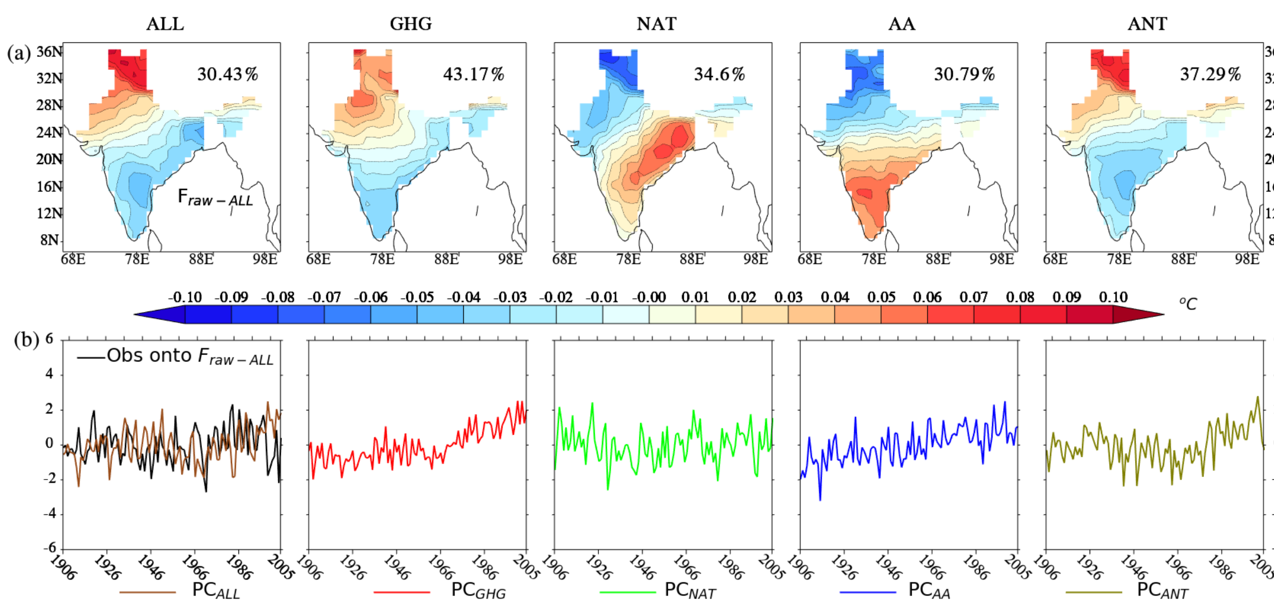

Figure S12: Same as Figure S10, but for spatial mean removed case.

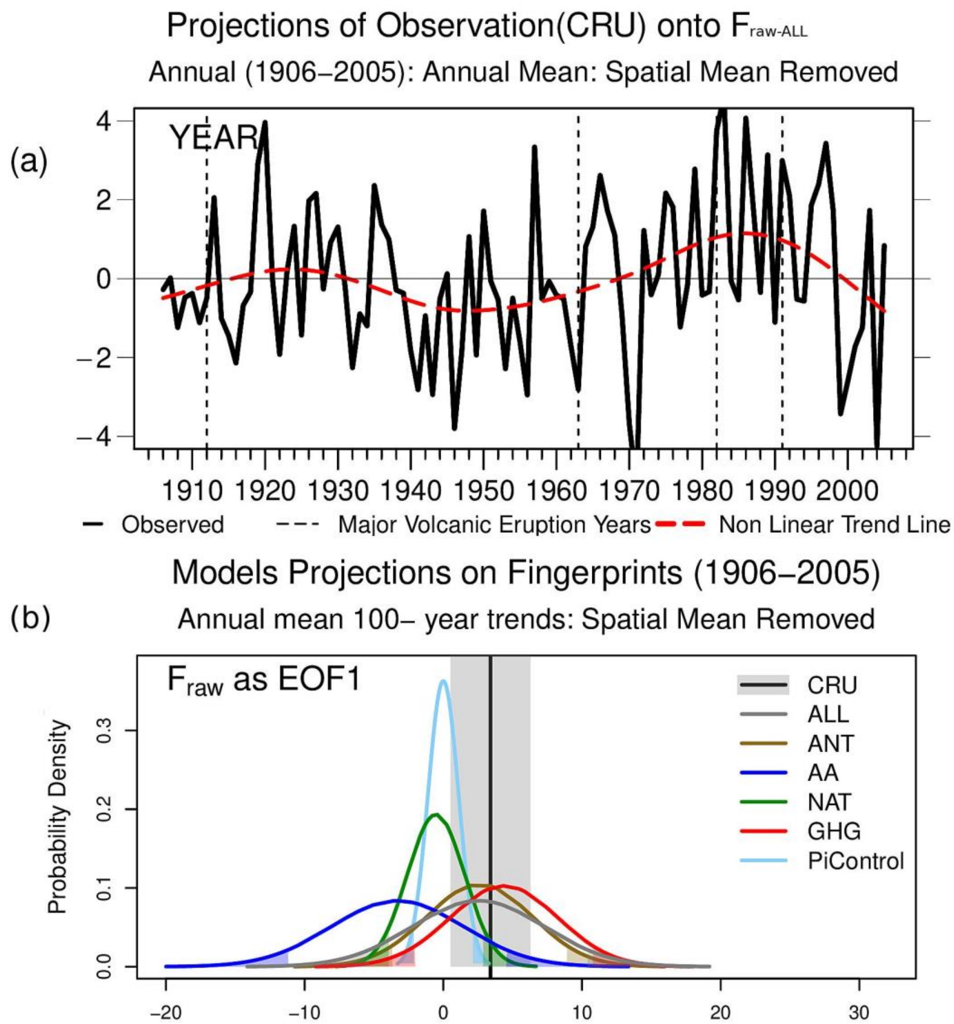

Figure S13: Same as Figure S11, but for the spatial mean removed case.

References

Scinocca, J. F., Stephenson, D. B., Bailey, T. C., & Austin, J. (2010). Estimates of past and future ozone trends from multimodel simulations using a flexible smoothing spline methodology. *Journal of Geophysical Research: Atmospheres*, *115*(D3).

Wood, S. N. *Generalized Additive Models: An Introduction with R.* CRC/Chapman & Hall, Boca Raton, FL, USA, 2006